

Phonon-assisted relaxation and decoherence of singlet-triplet qubits in Si/SiGe quantum dots

Viktoriia Kornich^{1,2}, Christoph Kloeffel¹, and Daniel Loss^{1,3}

¹Department of Physics, University of Basel, Klingelbergstrasse 82, CH-4056 Basel, Switzerland

²Department of Physics, University of Wisconsin–Madison, Madison, Wisconsin 53706, USA

³CEMS, RIKEN, Wako, Saitama 351-0198, Japan

May 25, 2018

We study theoretically the phonon-induced relaxation and decoherence of spin states of two electrons in a lateral double quantum dot in a SiGe/Si/SiGe heterostructure. We consider two types of singlet-triplet spin qubits and calculate their relaxation and decoherence times, in particular as a function of level hybridization, temperature, magnetic field, spin orbit interaction, and detuning between the quantum dots, using Bloch-Redfield theory. We show that the magnetic field gradient, which is usually applied to operate the spin qubit, may reduce the relaxation time by more than an order of magnitude. Using this insight, we identify an optimal regime where the magnetic field gradient does not affect the relaxation time significantly, and we propose regimes of longest decay times. We take into account the effects of one-phonon and two-phonon processes and suggest how our theory can be tested experimentally. The spin lifetimes we find here for Si-based quantum dots are significantly longer than the ones reported for their GaAs counterparts.

1 Introduction

Quantum dots (QDs) populated by electrons or holes are considered to be promising platforms for the physical realization of qubits for quantum computation [1–3]. Much progress both in theory and experiment was made in studying GaAs-based QDs [4–22]. However, recently Si- or Ge-based QDs attracted much attention. The reason is that in isotopically purified ²⁸Si or isotopes of Ge with nuclear spin 0 (e.g. ⁷⁶Ge) decoherence sources characteristic to GaAs are absent, namely hyperfine interaction and spin orbit interaction (SOI) due to lattice-inversion asymmetry. Known schemes for spin qubits in Si or Ge are based on, e.g., hole spins in CMOS devices [23], hut wires [24], and Ge-Si core-shell nanowires [25–29], donor electron spins [30–34], host [35] and donor [36–41] nuclear spins, nuclear-electron spin

qubits (Si:Bi) [42], qubits based on Si/SiO₂ structures [43–45], and lateral QDs within the two-dimensional electron gas (2DEG) in Si/SiGe heterostructures [46–51]. The sixfold degeneracy of conduction band valleys in Si can be an additional source of decoherence [52, 53] compared to GaAs. However, four of the six valleys get split off by a large energy of the order of a hundred meV in SiGe/Si/SiGe quantum wells because of the strain [53–56]. Due to confinement, which may also be varied via electric fields, the twofold degeneracy of the remaining valleys is lifted, and reported valley splittings are of the order of 0.1–1 meV [55–59]. For instance, electric control over the valley splitting for QDs in Si/SiO₂ was reported, and the presented energy range for the valley splitting is 0.3–0.8 meV [59]. Therefore, it is possible to suppress the effect of many valleys in Si if the energies characteristic for the qubit subspace are small enough.

Following the development in theory and experiment investigating the behavior of electron spin states in single and double quantum dots in Si [44, 46–53, 56–73], we study a lateral double quantum dot (DQD) which is formed in a Si/SiGe heterostructure and occupied by two electrons. We consider the relaxation and decoherence of the two-electron spin states due to phonons. Given the recent high interest in spin qubits at the S - T_- anticrossing [18, 74], where S is a spin singlet and T_- a spin triplet with magnetic quantum number $m = -1$ for the spin component along the quantization axis, we investigate how the relaxation time T_1 and the decoherence time T_2 of such qubits depend on temperature for different kinds of hybridization of the singlet. We derive and analyze the dependence of T_1 and T_2 on the magnetic field gradient, which is usually applied in order to operate the spin qubits [18, 47, 75, 76]. We further study the effects of one-phonon and two-phonon processes and suggest regimes where our theory can be tested experimentally. We also consider the S - T_0 spin qubit [5, 10, 11] in two regimes: large detuning and small detuning, as it was done in our previous work on DQDs in GaAs/AlGaAs [77]. Here, T_0 is the spin triplet with $m = 0$. We investigate the dependence of T_1 and T_2 on temperature and on different system parameters which were not considered before.

The paper is organized as follows. In Sec. 2, we present the Hamiltonian of our model and a short description of the Bloch-Redfield theory. In Sec. 3, we study the relaxation and decoherence of S - T -based spin qubits. The case of S - T_0 spin qubits is discussed in Sec. 4. Additional decay channels for the studied qubits are listed in Sec. 5 and our conclusions follow in Sec. 6.

2 Model

2.1 Hamiltonian

We consider lateral DQDs in a Si/SiGe heterostructure grown along the crystallographic direction [001], which we also denote as the z direction. The confinement in the plane perpendicular to z is generated by the gates. The homogeneous magnetic field \mathbf{B} is in this plane. An applied magnetic field gradient, which is usually produced via a micromagnet, enables control over the Bloch sphere of the spin qubit even in the absence of hyperfine and spin orbit interactions [18, 47, 75, 76].

The Hamiltonian of the system reads

$$\tilde{H} = \sum_{j=1,2} \left(H_0^{(j)} + H_Z^{(j)} + \tilde{H}_{SOI}^{(j)} + H_b^{(j)} + H_{el-ph}^{(j)} \right) + H_C + H_{ph}, \quad (1)$$

where j labels the electrons, H_0 comprises the kinetic and potential energy of an electron in a DQD potential, H_Z is the Zeeman term due to the external magnetic field, \tilde{H}_{SOI} is the spin orbit interaction after a suitable transformation that accounts for the effect of higher-energy states [78–82], H_b is the term that describes the effect of the applied magnetic field gradient, H_{el-ph} is the electron-phonon interaction, H_C is the Coulomb repulsion, and H_{ph} is the Hamiltonian of the phonon bath. The details and definitions of Eq. (1) are presented in Ref. [77] (Sec. II and Appendix B), except for the applied magnetic field gradient and the electron-phonon interaction Hamiltonian which we provide below in general form for one electron.

The applied magnetic field gradient acts on electrons similarly to the stabilized nuclear polarization in GaAs DQDs that produces a different Overhauser field for each QD. The Hamiltonian is therefore of the same form as for the hyperfine interaction and reads

$$H_b = \frac{\mathbf{b} \cdot \boldsymbol{\sigma}}{4} (\mathcal{P}_L - \mathcal{P}_R), \quad (2)$$

where \mathbf{b} appears due to the magnetic field gradient between the QDs, $\boldsymbol{\sigma}$ is the vector of Pauli matrices for the electron spin, and \mathcal{P}_L and \mathcal{P}_R are projectors for the left and right QD, respectively [77].

Now we consider the electron-phonon interaction in Si. In stark contrast to GaAs, only the deformation potential

electron-phonon interaction is present in Si. Another important difference is that the conduction band minimum in bulk Si is sixfold degenerate. However, because of the strain in SiGe/Si/SiGe quantum wells this sixfold degeneracy is lifted and there are only two degenerate valleys of lowest energy [53–56]. These two minima in the conduction band are found at the wave vectors $\mathbf{k}_{+z} = k_0 \mathbf{e}_z$ and $\mathbf{k}_{-z} = -k_0 \mathbf{e}_z$, where \mathbf{e}_z is the unit vector along the z direction, i.e., the [001] direction, and $k_0 \simeq 9.5 \text{ nm}^{-1}$ [55]. The confinement, tunable by electric fields, lifts the last degeneracy, and in good approximation the two z valleys at $\mathbf{k}_{\pm z}$ are the only valleys involved in the low-energy electron states [53, 55–57]. Therefore, following Refs. [83, 84], the electron-phonon Hamiltonian for our system reads

$$H_{el-ph} = \Xi_d \text{Tr} \boldsymbol{\varepsilon} + \Xi_u \mathbf{e}_z \cdot \boldsymbol{\varepsilon} \cdot \mathbf{e}_z. \quad (3)$$

Here, $\boldsymbol{\varepsilon}$ is a strain tensor defined as

$$\varepsilon_{ij} = \frac{1}{2} \left(\frac{\partial u_i}{\partial r_j} + \frac{\partial u_j}{\partial r_i} \right), \quad (4)$$

where i, j denote the spatial components, \mathbf{r} is the position in the material, and \mathbf{u} is the displacement operator. The trace of the strain tensor is $\text{Tr} \boldsymbol{\varepsilon}$. We note that the electron-phonon Hamiltonian of Eq. (3) is equivalent to

$$H_{el-ph} = \Xi_d \text{Tr} \boldsymbol{\varepsilon} + \Xi_u \varepsilon_{zz}. \quad (5)$$

The displacement operator can be represented in the form [77]

$$\mathbf{u} = \sum_{\mathbf{q}, s} \sqrt{\frac{\hbar}{2\rho V q v_s}} \mathbf{e}_{\mathbf{q}s} \left(a_{\mathbf{q}s} \mp_s a_{-\mathbf{q}s}^\dagger \right) e^{i\mathbf{q} \cdot \mathbf{r}}, \quad (6)$$

where $s \in \{l, t_1, t_2\}$ stands for the longitudinal and transverse acoustic modes, \mathbf{q} is a wave vector within the first Brillouin zone, and $q = |\mathbf{q}|$. We choose the normalized polarization vectors such that $\mathbf{e}_{\mathbf{q}l} = \mathbf{q}/q$, $\mathbf{e}_{-\mathbf{q}t_1} = -\mathbf{e}_{\mathbf{q}t_1}$, $\mathbf{e}_{-\mathbf{q}t_2} = \mathbf{e}_{\mathbf{q}t_2}$, and so $\mp_l = - = \mp_{t_1}$ and $\mp_{t_2} = +$. A phonon with properties \mathbf{q} and s is annihilated and created by the operators $a_{\mathbf{q}s}$ and $a_{\mathbf{q}s}^\dagger$, respectively. We note that the transverse phonons do not contribute to the term $\Xi_d \text{Tr} \boldsymbol{\varepsilon}$ in Eq. (5), they only contribute to $\Xi_u \varepsilon_{zz}$. For further calculations we use the density $\rho = 2.33 \text{ g/cm}^3$, the deformation potential constants [84] $\Xi_d = 5 \text{ eV}$ and $\Xi_u = 8.77 \text{ eV}$, and the averaged sound velocities [85, 86] $v_l = 9 \times 10^3 \text{ m/s}$, $v_{t_1} = v_{t_2} = 5.4 \times 10^3 \text{ m/s} = v_t$. Later on, when we calculate the qubit lifetimes, we can use the continuum limit and we integrate to infinite q for convenience, as terms with \mathbf{q} outside the first Brillouin zone do not affect our results for the temperatures considered here. The sample volume V will cancel out in the analysis.

We wish to emphasize that the results presented in this work cannot be obtained by simply replacing the parameters of our previous calculations [77] for GaAs DQDs, even

though several parts of the model can be adopted. The reason is that the electron-phonon interaction in Si fundamentally differs from that in GaAs or similar materials. In fact, we find that the novel term $\Xi_u \varepsilon_{zz}$ in Eq. (5) is crucial for the phonon-mediated decay of singlet-triplet qubits in Si DQDs.

2.2 Basis states and projected Hamiltonian

In this subsection we consider the Hamiltonian [Eq. (1)] in the basis $\{|(1,1)T_0\rangle, |(1,1)S\rangle, |(1,1)T_+\rangle, |(1,1)T_-\rangle, |(0,2)S\rangle, |(2,0)S\rangle\}$, where the first and second indices in parentheses correspond to the occupation number of the left and right QD, respectively, S denotes spin singlet states, and T denotes spin triplet states. As each minimum of the DQD potential in the plane of the 2DEG is well approximated by a 2D harmonic oscillator potential, we use linear combinations of the harmonic oscillator eigenfunctions to describe the in-plane orbital part of the electron state in the DQD potential [4]. For the explicit expressions of wave functions and details see Appendix A of Ref. [77]. Due to the strong confinement of the electrons in the growth direction, it turns out that the wave functions chosen along z hardly affect the phonon-assisted relaxation and decoherence processes that we are interested in. In contrast to Ref. [77], where a triangular potential based on typical GaAs/AlGaAs heterostructures was assumed, we consider a SiGe/Si/SiGe quantum well and

approximate it by a hard-wall potential

$$V(z) = \begin{cases} \infty, & z < 0, \\ C, & 0 < z < a_z, \\ \infty, & z > a_z, \end{cases} \quad (7)$$

where C is a constant with units of energy and $z = 0$, a_z corresponds to the interface between SiGe ($z < 0$, $z > a_z$) and Si ($0 < z < a_z$). The ground state wave function in such a potential is

$$\phi_z(z) = \sqrt{\frac{2}{a_z}} \sin \left[\frac{\pi z}{a_z} \right], \quad (8)$$

with a_z being a positive length that is interpreted as the width of the 2DEG in z direction. We take $a_z = 6$ nm for all numerical calculations in this work. We note that in experiments an electric field is usually applied along the growth direction of Si/SiGe heterostructures, which changes the shape of the assumed quantum well potential from rectangular toward triangular. However, as the electrons are strongly confined along z , the details of the well hardly affect the qubit lifetimes and we find that our results do not change by more than $\sim 10\%$ when the potential becomes completely triangular. As a consequence, our theory is also well applicable to, e.g., lateral Si DQDs formed in Si/SiO₂ systems.

The Hamiltonian in our basis reads

$$\tilde{H} = \begin{pmatrix} P_T & \frac{b_B}{2} & 0 & 0 & 0 & 0 \\ \frac{b_B}{2} & V_+ - V_- + P_T & \frac{\Omega}{\sqrt{2}} - \frac{1}{2\sqrt{2}}(b_x + ib_z) & -\frac{\Omega}{\sqrt{2}} + \frac{1}{2\sqrt{2}}(b_x - ib_z) & -\sqrt{2}t + P_S^\dagger & -\sqrt{2}t + P_S \\ 0 & \frac{\Omega}{\sqrt{2}} - \frac{1}{2\sqrt{2}}(b_x - ib_z) & E_Z + P_T & 0 & 0 & 0 \\ 0 & -\frac{\Omega}{\sqrt{2}} + \frac{1}{2\sqrt{2}}(b_x + ib_z) & 0 & -E_Z + P_T & 0 & 0 \\ 0 & -\sqrt{2}t + P_S & 0 & 0 & -\epsilon + U - V_- + P_{SR} & 0 \\ 0 & -\sqrt{2}t + P_S^\dagger & 0 & 0 & 0 & \epsilon + U - V_- + P_{SL} \end{pmatrix} + H_{ph}, \quad (9)$$

where t is the tunnel coupling, U is the onsite repulsion, V_+ and V_- are the matrix elements of Coulomb interaction, and $E_Z = g\mu_B B$ is the Zeeman splitting with $B = |\mathbf{B}|$, the Bohr magneton μ_B , and $g = 2$ as the electron g -factor in Si. The terms b_x , b_z , and b_B are produced by an applied magnetic field gradient along the x , z axes and \mathbf{B} , respectively, where the three orthogonal directions for x , z , and \mathbf{B} form a right-handed basis (meaning that \mathbf{B} points in the negative y direction, given that the axes x , y , z belong to a right-handed coordinate system). For simplicity, we set $b_z = 0$ in the following, as it can be achieved experimentally using a micromagnet. The electrical bias (detuning) between the dots is denoted by ϵ , where $\epsilon = 0$ is for the unbiased DQD [87].

The electron-phonon matrix elements are

$$P_T = \langle (1,1)S | \sum_{j=1,2} H_{el-ph}^{(j)} | (1,1)S \rangle = \langle (1,1)T_0 | \sum_{j=1,2} H_{el-ph}^{(j)} | (1,1)T_0 \rangle, \quad (10)$$

$$P_S = \langle (1,1)S | \sum_{j=1,2} H_{el-ph}^{(j)} | (2,0)S \rangle = \langle (0,2)S | \sum_{j=1,2} H_{el-ph}^{(j)} | (1,1)S \rangle, \quad (11)$$

$$P_{SR} = \langle (0,2)S | \sum_{j=1,2} H_{el-ph}^{(j)} | (0,2)S \rangle, \quad (12)$$

$$P_{SL} = \langle (2,0)S | \sum_{j=1,2} H_{el-ph}^{(j)} | (2,0)S \rangle. \quad (13)$$

As evident from the provided equations, these matrix elements have a similar structure but differ due to the integrals for the orbital parts. We note that the matrix elements all commute with each other, even though they still contain the creation and annihilation operators for the phonons.

The matrix element Ω comes from SOI and has the form [77, 82]

$$\Omega = \frac{F(L, l_c) g \mu_B B}{l_R} \cos \eta. \quad (14)$$

The function $F(L, l_c)$ depends on the distance L between the centers of the QDs and the confinement length $l_c = \sqrt{\hbar^2 / (m_{\text{eff}} \Delta E)}$, where $m_{\text{eff}} = 1.73 \times 10^{-31}$ kg is the transverse effective mass of an electron in Si and ΔE is the orbital level spacing in each QD. We note that l_c determines the Gaussian decay of the wave functions and $F(L, l_c) \approx -L$ when the dots are only weakly coupled. The Rashba length $l_R = \hbar / (m_{\text{eff}} \alpha)$ is related to the SOI amplitude α in the Rashba Hamiltonian, and η is the angle between \mathbf{B} and the axis that connects the two QDs.

2.3 Bloch-Redfield theory

To calculate the relaxation time T_1 and decoherence time T_2 we use the Bloch-Redfield theory [80, 88, 89], which describes the dynamics of the qubit interacting with the bath of phonons. The Bloch-Redfield formalism makes use of a Markov approximation, which is very well justified for our system because the qubit lifetimes T_1 and T_2 are several orders of magnitude longer than the correlation time τ_c . The latter can be estimated by considering the maximal duration which a phonon needs to travel through the DQD [80]. With the parameters used in the present work, this estimate yields $\tau_c \lesssim (L + 2l_c) / v_t \approx 0.04$ ns.

In the following we will consider $S-T_-$ and $S-T_0$ qubits. To decouple the qubit subspace from the other states, we first apply a unitary transformation to \tilde{H} that diagonalizes $\tilde{H} = H_{\text{el-ph}}^{(1)} - H_{\text{el-ph}}^{(2)}$, where (1) and (2) label the first and second electron, respectively. The transformation matrix for this first step is found numerically. Depending on the qubit under study ($S-T_0$ or $S-T_-$), we then perform a Schrieffer-Wolff transformation up to the third order to take into account both one-phonon and two-phonon processes. The Schrieffer-Wolff transformation corresponds to quasi-degenerate perturbation theory [90]. It is valid when the matrix elements resulting from electron-phonon coupling are much smaller than the energy difference between the qubit subspace and other states. After the Schrieffer-Wolff transformation, the qubit subspace is well separated from other states, which allows us to study the dynamics in terms of an effective Hamiltonian of the form $H_q + H_{q-ph}(\tau) + H_{ph}$, where H_q is a 2×2 part that contains information about the qubit without phonons and $H_{q-ph}(\tau)$ is the interaction between qubit and phonons at time τ in the interaction representation.

Defining the pseudo-spin vector $\tilde{\sigma}$ as a vector of Pauli matrices $\sigma_{\tilde{x}}, \sigma_{\tilde{y}}, \sigma_{\tilde{z}}$ in the qubit subspace, where $\tilde{x}, \tilde{y}, \tilde{z}$ are the directions in the pseudo-spin space, we can represent H_q and $H_{q-ph}(\tau)$ as

$$H_q = B_{\text{eff}} \sigma_{\tilde{z}}, \quad (15)$$

$$H_{q-ph}(\tau) = \delta \mathbf{B}(\tau) \cdot \tilde{\sigma}, \quad (16)$$

where B_{eff} is a positive energy and $\delta \mathbf{B}(\tau)$ contains electron-phonon interaction matrix elements. The expressions for B_{eff} and $\delta \mathbf{B}(\tau)$ result from all linear transformations performed before and are newly calculated whenever the input parameters or the qubit type change. Following the theory from Refs. [80, 89], the times T_2 and T_1 are

$$\frac{1}{T_2} = \frac{1}{2T_1} + \frac{1}{T_\varphi}, \quad (17)$$

$$\frac{1}{T_1} = J_{\tilde{x}\tilde{x}}^+(\Delta_{ST}) + J_{\tilde{y}\tilde{y}}^+(\Delta_{ST}), \quad (18)$$

$$\frac{1}{T_\varphi} = J_{\tilde{z}\tilde{z}}^+(0). \quad (19)$$

The quantity Δ_{ST} is defined as $\Delta_{ST} = 2B_{\text{eff}}$, i.e., the energy splitting between qubit states without taking into account electron-phonon interaction, and

$$J_{ii}^+(\hbar\omega) = \frac{2}{\hbar^2} \int_{-\infty}^{\infty} \cos(\omega\tau) \langle \delta B_i(0) \delta B_i(\tau) \rangle d\tau. \quad (20)$$

The correlator $\langle \delta B_i(0) \delta B_i(\tau) \rangle$ is evaluated for a phonon bath in thermal equilibrium at temperature T . The time T_φ represents the pure dephasing part in the decoherence time T_2 .

2.4 Corrections from valley degrees of freedom

When analyzing electrons in Si, it is important to consider possible effects of the valley degrees of freedom. In particular, the presence of more than one valley can have notable effects when excited states, which differ from the ground state by more than just the spin part, are occupied. For instance, this applies to singlet-triplet qubits in a single QD. When the qubit is in the triplet state, the two electron spins are parallel. Consequently, because of the Pauli exclusion principle, one of the two electrons must occupy an excited state. Compared with the ground state of the QD, the occupied excited state may differ in the valley or in the orbital part. In such systems, it therefore matters whether the orbital level spacing is smaller or greater than the valley splitting [52, 59].

In the present work we study singlet-triplet qubits in a DQD instead of a single QD. Compared with the latter, the choice between the left and the right QD of the DQD provides an additional degree of freedom. Therefore, in the limit where the two QDs have zero overlap, two electrons in the DQD can be in spin singlet and triplet states by always occupying the ground states of the QDs as far as the valley and

orbital degrees of freedom are concerned. Our work focuses on singlet-triplet qubits which are based on the low-energy eigenstates of two electrons in a DQD with weakly coupled QDs ($L > 2l_c$), such that the Hund-Mulliken approach is applicable [4, 87]. Consequently, it is not important in our model whether excited states in the QDs feature an excitation of orbital or valley type. There is only one exception where we will make the assumption that the valley splitting is larger than the orbital level spacing, see Sec. 4.2. While also the opposite case is possible [52, 59], we note that the assumption we will make in Sec. 4.2 was made in earlier calculations [52, 60] and that the realization of this regime has already been reported [58].

When studying the qubit decay in coupled Si QDs, using basis states without a valley degree of freedom (as in GaAs) is usually considered as a reasonable approximation [91, 92]. Provided that the valley splitting is large, which is feasible given the recent experimental progress [55–59], we therefore omit the valley degree of freedom in our calculations. If details about the valleys and the splittings are known, our model may be extended by choosing a larger set of basis states that takes the valleys into account [93]. As long as the valley splitting corresponds to a large quantity, however, we believe that inclusion of the valley states cannot lead to qubit lifetimes that are significantly shorter than those presented here. For corrections from additional decay mechanisms, we refer to Sec. 5.

3 $S-T_-$ qubit

Experimental and theoretical studies with two electrons in GaAs DQDs have shown that the $S-T_+$ anticrossing is useful for quantum information processing [18, 94–97]. For instance, a scheme has been proposed where single-spin rotations are performed at the center of the $S-T_+$ anticrossing [18]. One of the two electron spins serves as an ancillary spin in this scheme, and short gate times of a few nanoseconds were calculated for realistic setups with a micromagnet. Since the electron g -factor is negative in GaAs but positive in Si, such schemes which are based on the $S-T_+$ anticrossing in GaAs DQDs may easily be transferred to the $S-T_-$ anticrossing in Si DQDs [75]. Moreover, high gate fidelities have recently been predicted for singlet-triplet qubits in Si DQDs operated at the center of the $S-T_-$ anticrossing [74]. An advantage of the anticrossing is that $\partial\Delta_{ST}/\partial\epsilon \simeq 0$ near its center, and so the qubit is to a certain extent protected against charge noise [18, 74], especially when the anticrossing region is relatively wide.

Following the interest in building a qubit based on the $S-T_-$ anticrossing [18, 74] we study phonon-induced relaxation and decoherence for the electron spin states at this anticrossing. Because of tunnel coupling, magnetic field gradient, and SOI all the states in our basis are hybridized to

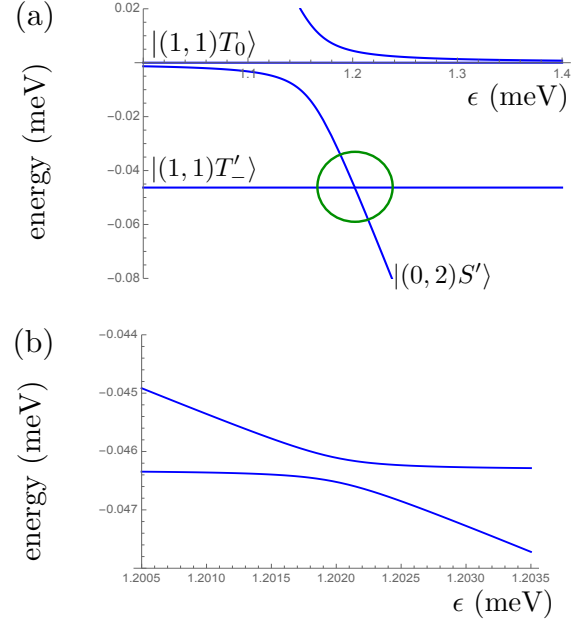


Figure 1: The energy spectrum of two-electron states in a double quantum dot as a function of detuning ϵ denoting the energy difference between the two dots. The green circle in panel a shows the $S-T_-$ anticrossing, which is shown enlarged in panel b. The parameters used are the same as for Fig. 3. At the anticrossing, the singlet state is of type $|(0,2)S'$.

some extent. We therefore consider two possible regimes: the state that mainly consists of $|(1,1)T_- \rangle$ (we denote it as $|(1,1)T'_- \rangle$) anticrosses with the state that is mainly $|(0,2)S' \rangle$ ($|(0,2)S'' \rangle$) or mainly $|(1,1)S' \rangle$ ($|(1,1)S'' \rangle$). This can also be seen from the spectrum. In Fig. 1a we plotted the dependence of the energy of two-electron states on the detuning ϵ . The green circle highlights the region of anticrossing between $|(1,1)T'_- \rangle$ and $|(0,2)S' \rangle$, which is shown enlarged in Fig. 1b. In Fig. 2 we choose different parameters and show the anticrossing between $|(1,1)T'_- \rangle$ and $|(1,1)S' \rangle$. When plotting these spectra, the electron-phonon interaction was omitted.

3.1 The qubit based on $|(1,1)T'_- \rangle$ - $|(0,2)S' \rangle$

Here we study the case shown in Fig. 1.

3.1.1 Dependence on temperature

We plot the dependence of T_1 and T_2 on temperature T in Fig. 3, for which we used the following parameters: $B = 0.4$ T, $t = 10$ μ eV, $V_+ = 40$ μ eV, $V_- = 39.99$ μ eV, $U = 1.2$ meV, $b_x = 2$ μ eV, $L = 150$ nm, $l_c = 42.7$ nm (i.e., $\Delta E = 200$ μ eV), and $\epsilon = 1.201988$ meV. The region where $|(1,1)T'_- \rangle$ and $|(0,2)S' \rangle$ anticross is typically quite narrow, and therefore such a high precision in ϵ is needed to

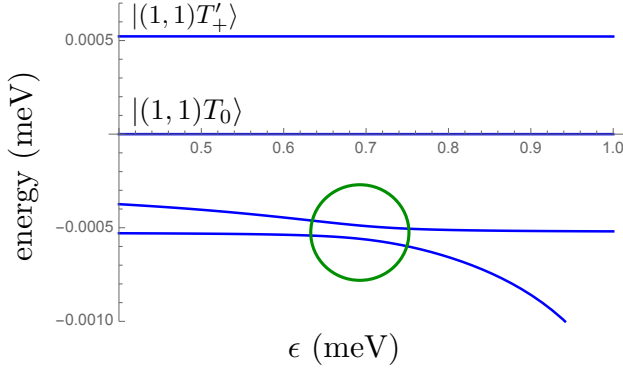


Figure 2: The energy spectrum of two-electron states in a double quantum dot as a function of detuning ϵ . The green circle shows the S - T_- anticrossing. The parameters used are the same as for Fig. 9. At the anticrossing, the singlet state is of type $|(1,1)S\rangle$.

operate exactly in the anticrossing center. That is the point where, if we take $b_x - 2\Omega = 0$, the energies of $|(0,2)S'\rangle$ and $|(1,1)T'_-\rangle$ are equal, i.e., $|(0,2)S'\rangle$ and $|(1,1)T_-\rangle$ cross. We take $b_B = 0$ to decouple the qubit subspace from $|(1,1)T_0\rangle$ [74].

As SOI enters in Eq. (9) together with b_x , we neglect it assuming $|\Omega| \ll |b_x|$. In lateral SiGe/Si/SiGe QDs, SOI might be due to QD confinement or other applied electric fields, imperfections of the quantum well [98], or interface effects between two semiconductors [99, 100]. According to Ref. [98], the spin-orbit length is $l_R = 73 \mu\text{m}$. Using this value, we get $\Omega = -0.095 \mu\text{eV}$ from Eq. (14) when $\eta = 0$. The SOI due to interface effects between semiconductors is absent if the amount of atomic monolayers of Si is even [101]. However, experimental values for any of the three origins mentioned above are not known to us for present-day samples.

In Fig. 3 we see that $T_2 \simeq 2T_1$, that means the relaxation part dominates over dephasing in T_2 [see Eq. (17)]. Up to a temperature of $T = 0.08 \text{ K}$, both T_1 and T_2 decay slowly and then change their behavior to a more rapid decay. To explain this change at around $T \simeq 0.08 \text{ K}$ we plot the one-phonon process decoherence rate (Γ_2^{1p}) and two-phonon process decoherence rate (Γ_2^{2p}), see Fig. 4. These rates contribute to T_2 as

$$\frac{1}{T_2} = \Gamma_2 = \Gamma_2^{1p} + \Gamma_2^{2p}. \quad (21)$$

We note that the one-phonon process can lead only to relaxation, it cannot lead to dephasing [77]. Therefore $\Gamma_2^{1p} = \Gamma_1^{1p}/2$, where Γ_1^{1p} is the one-phonon process relaxation rate. From Fig. 4 we can see that $\Gamma_2^{1p} \propto T$ for the whole temperature range. This is so because the dominant terms in Γ_2^{1p} are

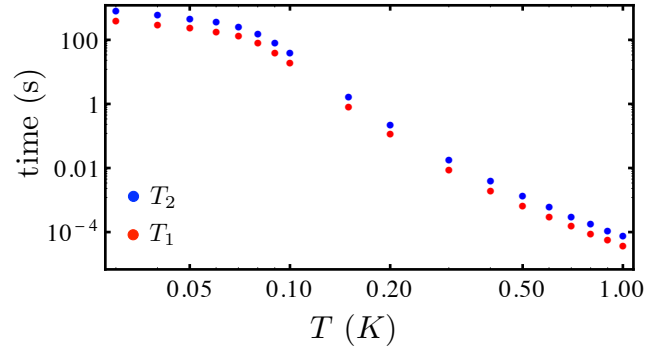


Figure 3: The dependence of T_1 (red) and T_2 (blue) on temperature for the parameters listed in Sec. 3.1.1. The anticrossing is between $|(1,1)T'_-\rangle$ and $|(0,2)S'\rangle$.

proportional to a Bose-Einstein distribution,

$$\Gamma_2^{1p} \propto (e^{\frac{\Delta_{ST}}{k_B T}} - 1)^{-1} \simeq \frac{k_B T}{\Delta_{ST}}. \quad (22)$$

In our case $\Delta_{ST} \ll k_B T$ for all temperatures under consideration, therefore the second equality in Eq. (22) is justified. The two-phonon process rate Γ_2^{2p} has a more complicated dependence on temperature. For $0.03 \text{ K} < T < 0.07 \text{ K}$, we find $\Gamma_2^{2p} \simeq C_1 + C_2 T^9$, where C_1 and C_2 are constants, then Γ_2^{2p} grows more slowly, and for $0.5 \text{ K} < T < 1 \text{ K}$ we obtain $\Gamma_2^{2p} \propto T^4$ in good approximation. Consequently, the change in the decay of T_1 and T_2 at $T \simeq 0.08 \text{ K}$ in Fig. 3 is due to the fact that for lower temperatures the relaxation happens mainly via one-phonon processes, with rate $\propto T$, and for higher temperatures two-phonon processes dominate with the rate depending on higher powers of T . The crossover between these two regimes occurs at around 0.08 K (see Fig. 4).

3.1.2 Dependence on the magnetic field gradient

As the magnetic field gradient is determined by the design of the experimental setup, we also plot the dependence of T_1 and T_2 on b_x , see Fig. 5. The parameter values we used are the same as for Fig. 3 and $T = 100 \text{ mK}$. Here again $T_2 \simeq 2T_1$. We can see a plateau up to $b_x \sim 2 \mu\text{eV}$ and then a decay for both T_1 and T_2 . To explain this behavior we study the dependence of Γ_2^{1p} and Γ_2^{2p} on b_x , see Fig. 6. Considering a fit function of the form $Y = C_i + C_{i+1} X^k$, as already used in Sec. 3.1.1, it turns out that $\Gamma_2^{1p} \simeq C_3 + C_4 b_x^4$, where C_3 and C_4 are constants. In contrast to Γ_2^{1p} , the rate Γ_2^{2p} does not change noticeably with b_x , and we will comment on this using a simple model in Sec. 3.1.4. Consequently, as for smaller b_x the rate Γ_2^{2p} dominates, there is a plateau in the regime of small b_x . For $b_x > 3 \mu\text{eV}$ the rate Γ_2^{1p} dominates, therefore both T_1 and T_2 decay.

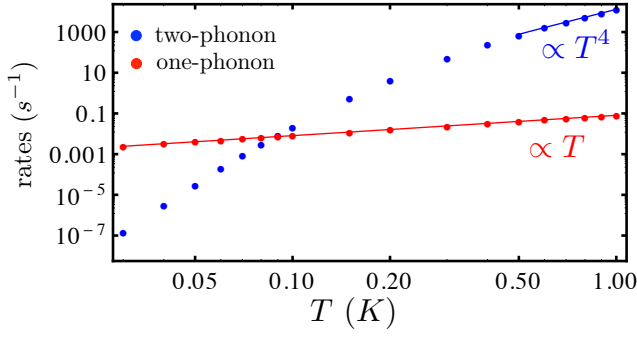


Figure 4: The dependence of one-phonon (Γ_2^{1p} , red) and two-phonon (Γ_2^{2p} , blue) components of the decoherence rate $1/T_2 = \Gamma_2^{1p} + \Gamma_2^{2p}$ on temperature. The straight lines obey the shown power-laws and are fits to the numerical data. The parameters are the same as in Fig. 3.

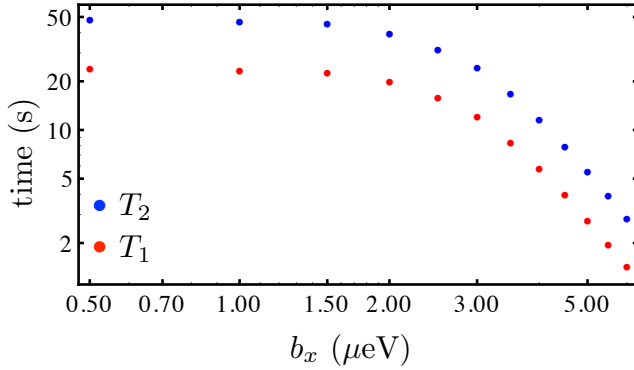


Figure 5: The dependence of T_1 (red) and T_2 (blue) on b_x . The temperature for this plot is $T = 100$ mK, and the other parameters are listed in Sec. 3.1.1. The anticrossing is between $|(1,1)T'_-\rangle$ and $|(0,2)S'\rangle$.

3.1.3 Proposed experiments to confirm the theory

In Fig. 3 we see that phonon-assisted relaxation and decoherence are slow compared to the ones usually reported for GaAs. Nevertheless, we found regimes where T_1 and T_2 are in the millisecond range, so that phonon-assisted relaxation and dephasing may dominate over other sources of decoherence in the sample. This provides an option to test our theory experimentally. We suggest to consider two cases: when the one-phonon process dominates and when the two-phonon process dominates.

To get the one-phonon process dominating, we use the following parameters: $b_x = 10 \mu\text{eV}$, $\epsilon = 1.173 \text{ meV}$, $T = 100 \text{ mK}$, and the other parameters are the same as for Fig. 3. This means we have a similar spectrum as in Fig. 1 and stay in the region to the left from the marked anticrossing to have a large splitting between the qubit states, which

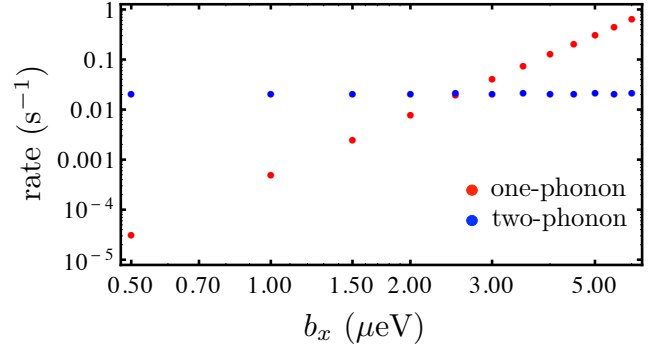


Figure 6: The dependence of one-phonon (Γ_2^{1p}) and two-phonon (Γ_2^{2p}) components of the decoherence rate $1/T_2 = \Gamma_2^{1p} + \Gamma_2^{2p}$ on b_x . The parameters are the same as in Fig. 5.

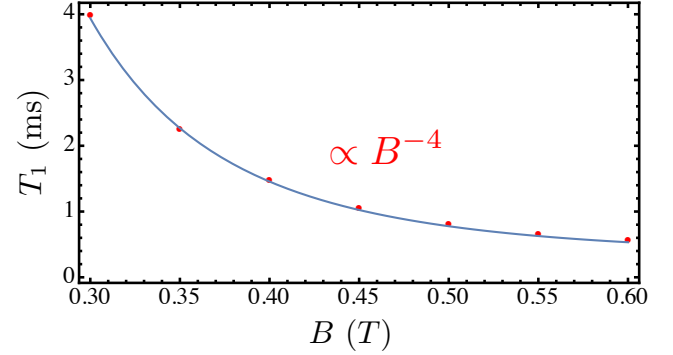


Figure 7: The dependence of T_1 on the absolute value B of the magnetic field for $T = 100 \text{ mK}$ and the parameters in the text. The blue line is a fit to the numerical results and shows a power-law decay $\propto B^{-4}$. The detuning ϵ was chosen near (but not exactly at) the anticrossing between $|(1,1)T'_-\rangle$ and $|(0,2)S'\rangle$.

increases the one-phonon relaxation rate. In Fig. 7 we plotted the dependence of T_1 on the applied magnetic field B . Here T_1 is mainly determined by the one-phonon process, therefore $T_1 \simeq 1/\Gamma_1^{1p}$. The decay scales as $T_1 \propto B^{-4}$. We note that we do not expect this power-law to be universal for all possible parameter values.

To test experimentally our theory of the two-phonon process, we suggest to change the magnetic field B around the value where we are exactly in the center of the anticrossing, and to use rather small b_x . We need b_x to be small enough, because at larger b_x the one-phonon process starts to dominate as evident from Fig. 6. Therefore, we use $b_x = 1 \mu\text{eV}$, $T = 500 \text{ mK}$, and the other parameters as for Fig. 3. We plot the B dependence of T_2 and T_1 in Fig. 8. Here we see a sharp peak for T_2 at $B = 0.4 \text{ T}$, which is the center of the anticrossing between $|(0,2)S'\rangle$ and $|(1,1)T'\rangle$.

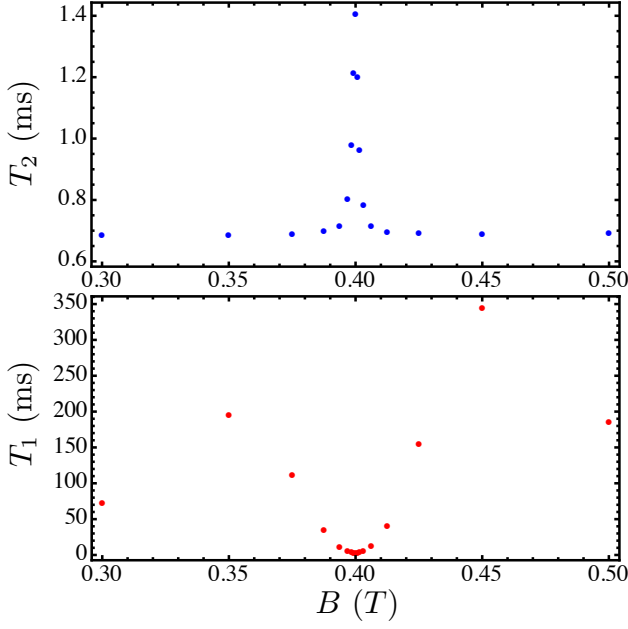


Figure 8: The dependence of T_2 and T_1 on the absolute value B of the magnetic field for $T = 500$ mK and the parameters in the text. The center of the anticrossing between $|(1,1)T'_-\rangle$ and $|(0,2)S'\rangle$ is at $B = 0.4$ T. The peak of T_2 at $B = 0.4$ T is limited by T_1 , i.e., $T_2 \simeq 2T_1$, whereas the valleys at $B < 0.395$ T, $B > 0.405$ T are predominantly determined by T_φ . In this figure, T_2 is due to two-phonon processes, one-phonon processes are negligible. For T_1 , two-phonon processes dominate at 0.375 T $< B < 0.425$ T.

Interestingly, dephasing is dominating for $B < 0.395$ T, $B > 0.405$ T, and the peak itself is limited by relaxation. The relaxation time T_1 is limited by two-phonon processes only at 0.375 T $< B < 0.425$ T. Apart from its usefulness for checking our theory of two-phonon processes the peak in T_2 (or dip in T_1) is a clear indication of the $|(0,2)S'\rangle$ and $|(1,1)T'_-\rangle$ anticrossing center, the point which is most interesting for spin qubit operation [18, 74].

Taking into account that the phonon-induced decoherence still allows for relatively long qubit lifetimes, we suppose that for the present-day samples the main source of decoherence in such a qubit will be charge noise, because the anticrossing region is quite narrow. However, as was discussed in Ref. [18], the charge noise can be substantially reduced using $t \gg E_Z$.

3.1.4 Simple model for the qubit based on $|(1,1)T'_-\rangle$ - $|(0,2)S'\rangle$

To analyze the results presented above, we propose to consider a simple model, which besides energy separation arguments discussed below is also justified by comparison with our numerical calculations. The states that are

closest in energy to our $|(1,1)T'_-\rangle$ - $|(0,2)S'\rangle$ qubit subspace are $|(1,1)T_0\rangle$ and $|(1,1)S'\rangle$. However, $|(1,1)T_0\rangle$ is decoupled from the qubit subspace when $b_B = 0$. Therefore we consider the Hamiltonian in the basis $\{|(1,1)T_-\rangle, |(0,2)S'\rangle, |(1,1)S'\rangle\}$:

$$\tilde{H} = \begin{pmatrix} -E_Z & 0 & \frac{1}{2\sqrt{2}}b_x \\ 0 & -\epsilon + U - V_- + \tilde{P} & -\sqrt{2}t + P_S \\ \frac{1}{2\sqrt{2}}b_x & -\sqrt{2}t + P_S^\dagger & V_+ - V_- \end{pmatrix} + H_{ph}, \quad (23)$$

where $\tilde{P} = P_{SR} - P_T$. Our numerical calculation also showed that P_S and P_S^\dagger can be neglected, therefore we will omit them in this subsection.

First of all we have to find the center of the $|(1,1)T'_-\rangle$ - $|(0,2)S'\rangle$ anticrossing. For that we diagonalize the phonon-independent part of \tilde{H} in the basis $\{|(0,2)S'\rangle, |(1,1)S'\rangle\}$. This transformation is [87]

$$U_1 = \begin{pmatrix} 1 & 0 & 0 \\ 0 & \cos(\phi/2) & -\sin(\phi/2) \\ 0 & \sin(\phi/2) & \cos(\phi/2) \end{pmatrix}, \quad (24)$$

where

$$\cos \phi = \frac{-U + V_+ + \epsilon}{\sqrt{8t^2 + (-U + V_+ + \epsilon)^2}}, \quad (25)$$

$$\sin \phi = \frac{2\sqrt{2}t}{\sqrt{8t^2 + (-U + V_+ + \epsilon)^2}}. \quad (26)$$

Consequently, the matrix $U_1^\dagger \tilde{H} U_1$, with U_1^\dagger as the conjugate transpose of U_1 , corresponds to the Hamiltonian \tilde{H} written in the basis $\{|(1,1)T_-\rangle, |(0,2)S'\rangle, |(1,1)S'\rangle\}$, if we set $b_x = 0$. The anticrossing center is the point where the energy of $|(1,1)T_-\rangle$ is equal to the energy of $|(0,2)S'\rangle$ (with $b_x = 0$ and $\tilde{P} = 0$). From this condition we find the detuning ϵ at which the anticrossing occurs,

$$\epsilon = E_Z + U - V_- - \frac{2t^2}{E_Z - V_- + V_+}. \quad (27)$$

Assuming that $|b_x|$, $|t|$, and \tilde{P} (may, e.g., be estimated via the expectation value of \tilde{P}^2) are much smaller than $\Delta = \sqrt{8t^2 + (U - V_+ - \epsilon)^2}$, we perform a Schrieffer-Wolff transformation up to the fourth order. The resulting Hamiltonian for the qubit and the phonons is then split into the part which does not contain phonons, the part with electron-phonon interaction, and H_{ph} . To simplify the analysis we apply to this Hamiltonian a unitary transformation U_2 which exactly diagonalizes the phonon-independent part,

$$U_2 = \begin{pmatrix} \cos(\Theta/2) & -\sin(\Theta/2) \\ \sin(\Theta/2) & \cos(\Theta/2) \end{pmatrix}, \quad (28)$$

where the angle Θ is defined as

$$\cos(\Theta/2) = \frac{c}{\sqrt{c^2 + 1}}, \quad (29)$$

$$\sin(\Theta/2) = \frac{1}{\sqrt{c^2 + 1}}, \quad (30)$$

and

$$c = \frac{4b_x\Delta^2(1 + \cos\phi) - b_x^3\cos^2(\frac{\phi}{2})\cos\phi + \sqrt{\cos^4(\frac{\phi}{2})b_x^2(b_x^2\cos\phi - 8\Delta^2)^2 + 2\Delta^2(b_x^2 - 32\Delta^2 + b_x^2\cos\phi)^2\sin^2(\frac{\phi}{2})}}{\sin(\frac{\phi}{2})\sqrt{2}\Delta(b_x^2 - 32\Delta^2 + b_x^2\cos\phi)}. \quad (31)$$

After all transformations our Hamiltonian is $H_q + H_{el-ph}(\tau) + H_{ph}$ as it was described in Sec. 2.3. Therefore, in order to understand the results from Sec. 3.1, we present here the expression for $\delta B_{\bar{x}}(\tau)$ which leads to relaxation and the one for $\delta B_{\bar{z}}(\tau)$ which leads to dephasing,

$$\delta B_{\bar{x}}(\tau) = \frac{1}{128\Delta^3} \left[\tilde{P}(\tau) \cos^2 \left[\frac{\phi}{2} \right] (G_1 \cos \Theta - G_2 \sin \Theta) + \tilde{P}^2(\tau) (G_3 \cos \Theta - G_4 \sin \Theta) \right], \quad (32)$$

$$\delta B_{\bar{z}}(\tau) = \frac{1}{128\Delta^3} \left[\tilde{P}(\tau) \cos^2 \left[\frac{\phi}{2} \right] (G_1 \sin \Theta + G_2 \cos \Theta) + \tilde{P}^2(\tau) (G_3 \sin \Theta + G_4 \cos \Theta) \right]. \quad (33)$$

We note that $\delta B_{\bar{y}}(\tau) = 0$, and we introduced

$$G_1 = \sqrt{2}b_x \sin \left[\frac{\phi}{2} \right] (b_x^2 + 32\Delta^2 - 7b_x^2 \cos \phi), \quad (34)$$

$$G_2 = 4\Delta (b_x^2 - 16\Delta^2 - b_x^2 \cos \phi), \quad (35)$$

$$G_3 = 2\sqrt{2}b_x \sin \phi \cos \left[\frac{\phi}{2} \right] (5\tilde{P}(\tau) - 4\Delta + 5\tilde{P}(\tau) \cos [2\phi] + [8\Delta - 6\tilde{P}(\tau)] \cos \phi), \quad (36)$$

$$G_4 = 16\Delta \sin^2 \phi (\Delta + \tilde{P}(\tau) \cos \phi) \quad (37)$$

for convenience. Using Eqs. (32) and (33) we get the expressions for $\delta B_{\bar{x}}(0)\delta B_{\bar{x}}(\tau)$ and $\delta B_{\bar{z}}(0)\delta B_{\bar{z}}(\tau)$. To simplify them we use the fact that $\Theta \simeq \pi/2$ and $\Delta \gg |b_x|$, and get

$$\delta B_{\bar{x}}(0)\delta B_{\bar{x}}(\tau) \simeq \frac{1}{64\Delta^2} \left[16 \cos^4 \left[\frac{\phi}{2} \right] \Delta^2 \tilde{P}(0)\tilde{P}(\tau) - 4 \cos^2 \left[\frac{\phi}{2} \right] \cos \phi \sin^2 \phi (\tilde{P}^3(0)\tilde{P}(\tau) + \tilde{P}(0)\tilde{P}^3(\tau)) + \sin^4 \phi \tilde{P}^2(0)\tilde{P}^2(\tau) \right], \quad (38)$$

$$\delta B_{\bar{z}}(0)\delta B_{\bar{z}}(\tau) \simeq \frac{1}{32\Delta^4} \cos^4 \left[\frac{\phi}{2} \right] \sin^2 \left[\frac{\phi}{2} \right] b_x^2 [\cos \phi (5 \cos \phi - 3) (\tilde{P}^3(0)\tilde{P}(\tau) + \tilde{P}(0)\tilde{P}^3(\tau)) + (2 \cos \phi - 1)^2 \tilde{P}^2(0)\tilde{P}^2(\tau)]. \quad (39)$$

The first term in the brackets in Eq. (38) is responsible for a one-phonon process, and the rest for two-phonon processes. We note that in the numerical calculations in this work we neglected terms of the type $\tilde{P}^3(0)\tilde{P}(\tau)$ and $\tilde{P}(0)\tilde{P}^3(\tau)$. The relaxation mechanism that results from these terms can be interpreted as a higher-order correction to the standard one-phonon process. In the presence of phonons which are neither absorbed nor emitted, one phonon matches the Zeeman energy and ensures energy conservation. Furthermore, analogous to the standard terms of a one-phonon process, such terms do not contribute to dephasing at all [77].

The coefficient of $\tilde{P}^2(0)\tilde{P}^2(\tau)$ in Eq. (38) is more than 1000 times larger than the coefficient of the same term in Eq. (39) for the parameter values we used for Fig. 3. This suggests that two-phonon-based dephasing is negligibly small compared to two-phonon-based relaxation, and explains why in Fig. 3 we have $T_2 \simeq 2T_1$. Qualitatively, the presented relaxation via two-phonon pro-

cesses can be understood as follows. At the anticrossing, the eigenstates of the qubit Hamiltonian are approximately $[(0, 2)S'] \pm [(1, 1)T_-] / \sqrt{2}$. Two-phonon Raman processes [102–106] based on the singlet states of the biased DQD [77, 107] efficiently shift the energy of $|(0, 2)S'\rangle$, which corresponds to a transverse coupling in the qubit subspace and therefore leads to relaxation.

From Eqs. (38) and (39) it is evident that the dephasing part depends on b_x strongly, whereas for relaxation b_x enters only with Δ_{ST} in $J_{\bar{x}\bar{x}}^+(\Delta_{ST})$. The explicit expressions for $\int_{-\infty}^{\infty} \cos(\Delta_{ST}\tau/\hbar) \langle \tilde{P}^2(0)\tilde{P}^2(\tau) \rangle d\tau$ show that Δ_{ST} enters in the dominating terms as $q + \Delta_{ST}/(\hbar v_l)$, where $\hbar q$ is the momentum of a phonon. The integrals over q (continuum limit) can simply be performed from 0 to ∞ and converge because of Bose-Einstein terms or because of the Gaussian terms that result when integrating out the spatial dependence of the electron wave functions combined with oscillations of type $e^{iq \cdot r}$. We note that these Gaussian terms have decayed

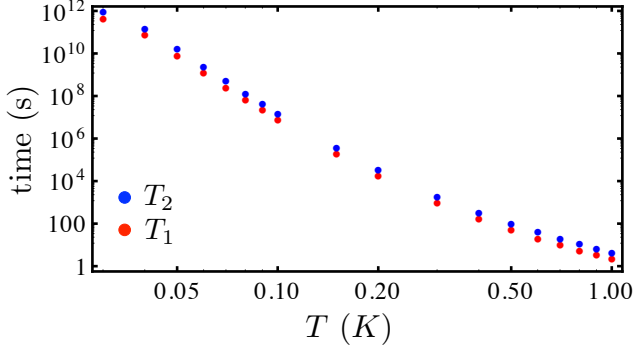


Figure 9: The dependence of relaxation time T_1 (red) and T_2 (blue) on temperature. The anticrossing is between $|(1,1)T'_-\rangle$ and $|(1,1)S'\rangle$. For the parameters, see Sec. 3.2.

when the phonon wavelength is (much) smaller than the size of a QD [80, 108, 109]. The main contribution to the rates is provided by the part of the integrals with $q \gg \Delta_{ST}/(\hbar v_l)$ within the range of parameters used for Figs. 3 and 5. Therefore, for the two-phonon relaxation process, the effect of b_x is negligible, which is seen in Fig. 6.

3.2 The qubit based on $|(1,1)T'_-\rangle$ - $|(1,1)S'\rangle$

Now let us consider the case where the qubit is based on the anticrossing $|(1,1)T'_-\rangle$ - $|(1,1)S'\rangle$, as shown in Fig. 2. For this, we plot the temperature dependence of T_1 and T_2 (see Fig. 9) using the following parameters: $B = 4.5$ mT, $t = 10$ μ eV, $V_+ = 40$ μ eV, $V_- = 39.99$ μ eV, $U = 1.2$ meV, $b_x = 0.1$ μ eV, $L = 150$ nm, $l_c = 42.7$ nm, $\epsilon = 0.68737$ meV. We see that again $T_2 \simeq 2T_1$. In Fig. 10 we plotted the dependence of Γ_2^{1p} and Γ_2^{2p} on temperature. The transition where the two-phonon process starts to dominate over the one-phonon process is now at lower temperature than for the case plotted in Fig. 4. We note that at 0.03 K $< T < 0.08$ K, a fit yields $\Gamma_2^{2p} \simeq C_5 + C_6 T^{10}$ for the two-phonon process rate, where C_5, C_6 are constants.

Remarkably, from Fig. 9 it follows that phonon-induced relaxation and decoherence are extremely slow. However, as we noted before, we neglected the effect of SOI in this calculation. When b_x is very small, it can be that SOI effects are noticeable. Let us assume there is Rashba SOI in our sample. Then, for the values of b_x, E_Z, L , and l_c we use in this subsection, the Rashba SOI length must be $l_R \simeq 1.6$ μ m for 2Ω to be of the same absolute value as b_x . We note that in GaAs/AlGaAs heterostructures l_R of the order of 1 μ m has been reported [2]. Although we are not aware of precise values for the SOI of electrons in lateral Si/SiGe-based QDs, we expect it to be weaker (l_R longer) than in GaAs/AlGaAs.

We note that the $|(1,1)T'_-\rangle$ - $|(1,1)S'\rangle$ -type qubit is also robust against charge noise, because the qubit is operated at

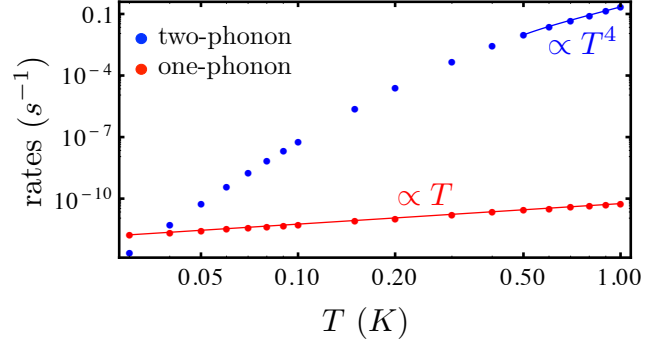


Figure 10: The dependence of one-phonon (Γ_2^{1p}) and two-phonon (Γ_2^{2p}) components of the decoherence rate on temperature. The anticrossing is between $|(1,1)T'_-\rangle$ and $|(1,1)S'\rangle$. The straight lines obey the shown power-laws and are fits to our numerical results. The parameters are the same as in Fig. 9.

the “sweet spot”, where $\partial\Delta_{ST}/\partial\epsilon \simeq 0$, and the anticrossing region is wide [74].

4 S - T_0 qubit

In this section we consider the qubit based on $|(1,1)S'\rangle$ - $|(1,1)T'_0\rangle$. There are two cases which we are interested in. The first one is the region of large detuning, where $|(0,2)S'\rangle$ is close to the qubit subspace. The second one is the zero-detuning case, where we have to take excited orbital states into account. We already considered these cases in our previous work on QDs in GaAs/AlGaAs heterostructures, Ref. [77]. Here we consider a QD in a SiGe/Si/SiGe quantum well and present the dependence of T_1 and T_2 on different quantities which were not studied in our previous work.

4.1 Large detuning

In this subsection we consider the region near the anticrossing of $|(1,1)S'\rangle$ and $|(0,2)S'\rangle$, where the state $|(0,2)S'\rangle$ is sufficiently closer to the qubit subspace than states with excited orbital parts, so that the latter can be omitted. We use the Hamiltonian from Eq. (9) and calculate T_1 and T_2 using the theory described in Sec. 2.3. At the end of this subsection we present a simple analytic model and discuss our numerical results.

4.1.1 Dependence on the magnetic field gradient

We study the dependence of T_1 and T_2 on the energy b_B associated with the magnetic field gradient. For Fig. 11 we used $B = 0.4$ T, $t = 4$ μ eV, $V_+ = 40$ μ eV, $V_- = 39.99$ μ eV, $U = 1.2$ meV, $b_x = 0$, $L = 150$ nm, $l_c =$

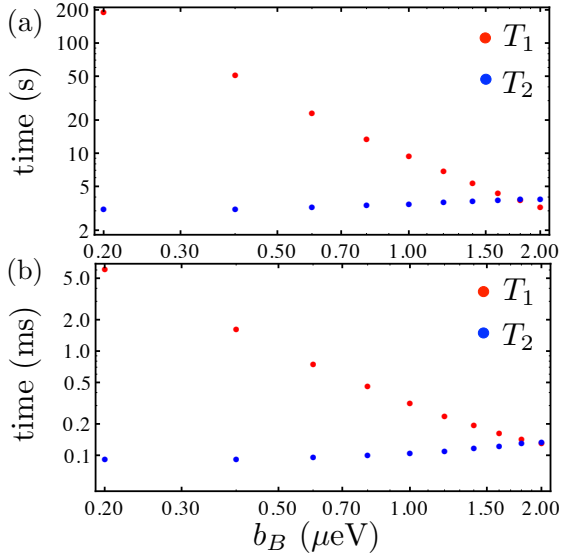


Figure 11: (a) The dependence of T_1 (red) and T_2 (blue) on b_B for a S - T_0 qubit at large detuning. The temperature is $T = 100$ mK. The decoherence time T_2 is slightly increasing (except for the last point) with increasing b_B , whereas the relaxation time decreases drastically. (b) The same dependence as in panel a, but at $T = 500$ mK. Other parameters are given in Sec. 4.1.1.

42.7 nm, and $\epsilon = 1.144$ meV. The chosen confinement length corresponds to the level splitting $\Delta E = 200$ μ eV, which allows us to neglect the effect of the excited states compared to $|(0, 2)S'\rangle$ due to the large energy gap. As we took $b_x = 0$, we consider non-zero Rashba SOI. The Rashba SOI length we use is quite short, $l_R = 2$ μ m, and we take $\eta = 0$ to make the effect of SOI maximal [see Eq. (14)], resulting in $\Omega = -3.48$ μ eV. However, our numerical calculation of the qubit lifetimes showed that the effect of SOI in this regime of large detuning, even with a rather small l_R and $\eta = 0$, is negligible. For the parameters described above and the range of b_B in Fig. 11, the resulting Δ_{ST} is in the range 1.8 μ eV $< \Delta_{ST} < 2.6$ μ eV.

From Fig. 11 we see that the behavior of T_1 and T_2 is similar at $T = 100$ mK and $T = 500$ mK. We note that in contrast to our previous work for GaAs QDs [77], the relation $T_\varphi \ll T_1$ does not hold for the whole parameter range. For $b_B < 0.8$ μ eV the pure dephasing part T_φ dominates over T_1 , bringing T_2 to much lower values than T_1 . However, as the magnetic field gradient enhances relaxation processes strongly, T_1 decays rapidly with b_B , becoming of the order of T_2 and even $T_1 < T_2$ for $b_B > 1.6$ μ eV. The strong dependence of relaxation on b_B is easy to understand from the Hamiltonian [Eq. (9)], because $b_B/2$ is the off-diagonal term between $|(1, 1)S\rangle$ and $|(1, 1)T_0\rangle$ and the only term that couples $|(1, 1)T_0\rangle$ to other states. This means that relaxation occurs only in case $b_B \neq 0$ and strongly depends on the

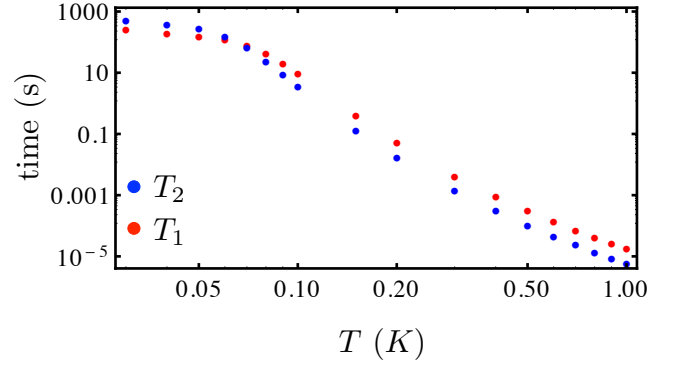


Figure 12: The dependence of T_2 (blue) and T_1 (red) on temperature T for a S - T_0 qubit at large detuning ϵ .

value of b_B . We obtain $T_1 \propto b_B^{-2}$ for $b_B < 1$ μ eV in Fig. 11 (both a and b).

4.1.2 Dependence on temperature

We also show the temperature dependence of T_1 and T_2 , see Fig. 12. For this plot we used $b_B = -1$ μ eV and otherwise the same parameters as for Fig. 11. The splitting between the qubit states $|(1, 1)S'\rangle$ and $|(1, 1)T'_0\rangle$ is $\Delta_{ST} \simeq 2$ μ eV. From Fig. 12 we see that both T_2 and T_1 , as expected, decrease with temperature. At very low temperatures, i.e., $T < 0.06$ K, $T_2 > T_1$. Then, however, T_2 decays faster than T_1 . For 0.5 K $\leq T \leq 1$ K, their power-laws are the same, $\propto T^{-4}$.

To understand why T_2 (similarly for T_1) decays so slowly for $T < 0.06$ K and then faster, we plot the temperature dependence of Γ_2^{1p} and Γ_2^{2p} (see Fig. 13). Here we see that for $T \leq 0.05$ K the one-phonon process dominates and $\Gamma_2^{1p} \propto T$, which gives a slow decay of T_1 and T_2 with temperature. The origin of this dependence of Γ_2^{1p} is the same as the one explained in Sec. 3.1.1. For temperatures $T \geq 0.1$ K the two-phonon process dominates. Therefore, as $\Gamma_2^{2p} \propto T^4$ for 0.5 K $\leq T \leq 1$ K, we see the same power-law for $1/T_2$. With a similar analysis for T_1 , we find that for 0.5 K $\leq T \leq 1$ K also $1/T_1 \propto T^4$ due to two-phonon processes. Since we have a rather large b_B , the dephasing part T_φ is of the same order as T_1 , as was shown in Sec. 4.1.1. The reason for choosing here a large b_B is the reported values for applied magnetic field gradients in experiments with micromagnets [18, 47, 75, 76].

4.1.3 Dependence on detuning

Here we show that in the anticrossing region even small changes of ϵ affect both T_1 and T_2 strongly. For that we present the dependence of T_1 and T_2 on ϵ , see Fig. 14, where we used the same parameters as for Fig. 11 and took $b_B = -1$ μ eV and $T = 100$ mK. For the range of ϵ

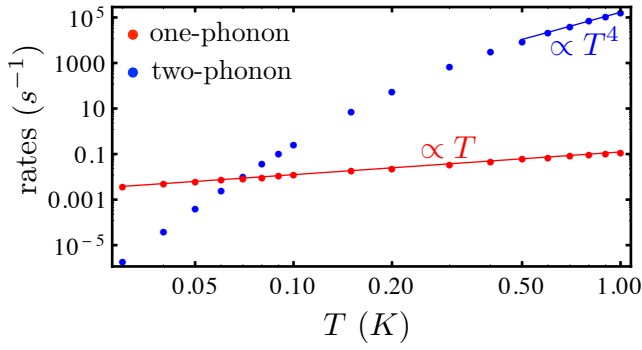


Figure 13: The dependence of one-phonon (Γ_2^{1p}) and two-phonon (Γ_2^{2p}) components of the decoherence rate on temperature T . The straight lines are fits to our numerical results and obey the indicated power-laws. The parameters are the same as for Fig. 12 and are provided in Sec. 4.1.

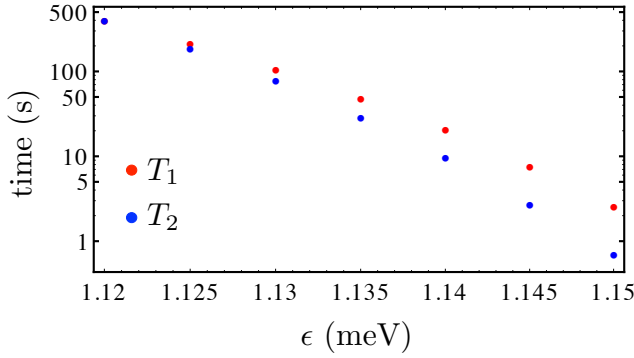


Figure 14: The dependence of T_1 (red) and T_2 (blue) on detuning ϵ for a S - T_0 qubit at $T = 100$ mK. Details are described in the text.

shown in Fig. 14 the splitting Δ_{ST} takes values in the range $1.3 \mu\text{eV} < \Delta_{ST} < 2.7 \mu\text{eV}$. We see that even though the change of ϵ is only $30 \mu\text{eV}$, the relaxation time and decoherence time both change drastically. The main reason for this behavior is that in this region $|(0, 2)S'\rangle$ very quickly drops in energy with ϵ and hence comes closer to the qubit subspace.

4.1.4 Dependence on tunnel coupling

To find the optimal regime for qubit operation we present the dependence of T_1 and T_2 on the tunnel coupling t between the dots, see Fig. 15. For this calculation we used $b_B = -1 \mu\text{eV}$ and the other parameters as for Fig. 11. The S - T_0 splitting changed with $3 \mu\text{eV} < t < 8 \mu\text{eV}$ in the interval $1.4 \mu\text{eV} < \Delta_{ST} < 5.9 \mu\text{eV}$. For Fig. 15a we used $T = 100$ mK and for Fig. 15b $T = 500$ mK. From Fig. 15a we

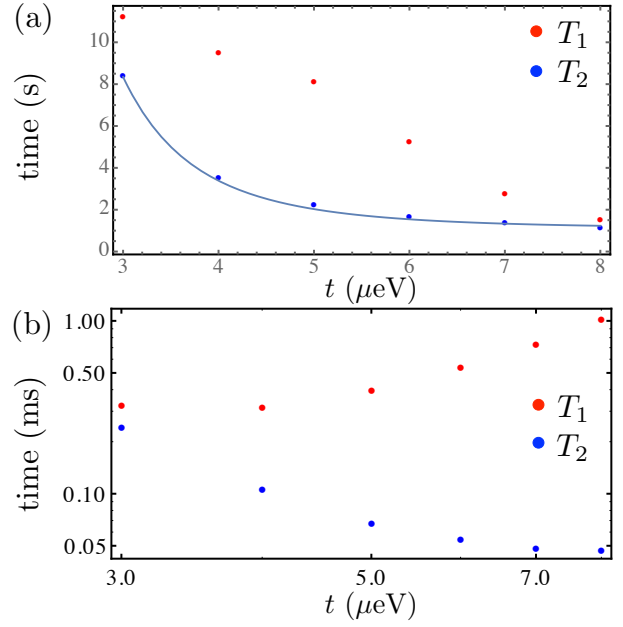


Figure 15: (a) The dependence of T_2 (blue) and T_1 (red) on the tunnel coupling t for a S - T_0 qubit in a biased DQD. Here the temperature is 100 mK, for the other parameters see Sec. 4.1. The blue line shows the fit with the function $T_2 = C_7 + C_8 t^{-4}$. Both T_1 and T_2 decay with t . (b) The same dependence as in panel a, but at a higher temperature $T = 500$ mK. Here we see that T_1 grows with t , in contrast to the case with $T = 100$ mK shown in panel a.

see that both T_1 and T_2 decay with t . However, the forms of their decays are different. The decay of T_2 reveals an approximate dependence $T_2 \simeq C_7 + C_8 t^{-4}$, where C_7 and C_8 are constants (the blue line in Fig. 15a). In Fig. 15b we see that T_2 decays with t . However, T_1 grows with t for $t > 4 \mu\text{eV}$.

To understand this behavior of T_1 we plot the dependence of relaxation rates due to one-phonon (Γ_1^{1p}) and two-phonon processes (Γ_1^{2p}) on t again for 100 mK and 500 mK (see Fig. 16). The rates satisfy

$$\frac{1}{T_1} = \Gamma_1 = \Gamma_1^{1p} + \Gamma_1^{2p}. \quad (40)$$

In both Figs. 16a (100 mK) and 16b (500 mK) the one-phonon rate grows with t , whereas the two-phonon rate slowly decays at $t > 4 \mu\text{eV}$. The difference in behavior of T_1 in Figs. 15a and 15b arises from the fact that for the lower temperature, i.e., 100 mK, for $t \geq 6 \mu\text{eV}$ the one-phonon relaxation rate dominates, which makes T_1 decrease with t . However, at larger temperature, $T = 500$ mK, the two-phonon process starts to dominate (see Fig. 16b), which makes T_1 grow with t .

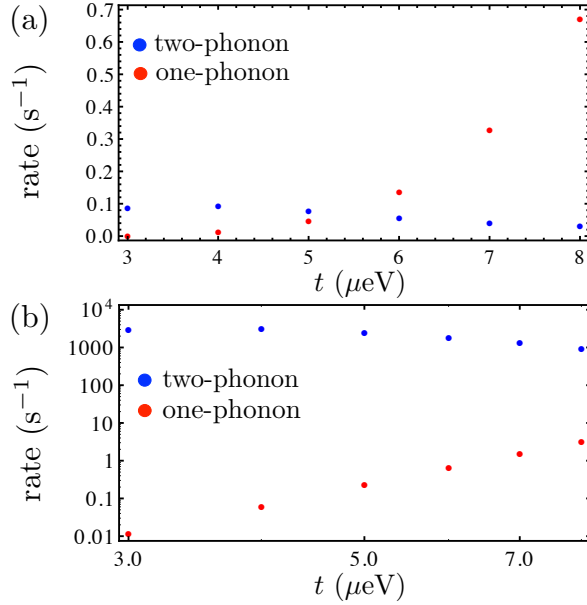


Figure 16: The dependence of relaxation rates due to one-phonon processes (Γ_1^{1p}) and two-phonon processes (Γ_1^{2p}) on the tunnel coupling t . The temperature is 100 mK in panel a and 500 mK in panel b. The parameters are the same as for Fig. 15.

4.1.5 Simple model for the S - T_0 qubit at large detuning

To understand the dependences on different parameters presented above, we consider a simple model. Similarly to the simple model of Ref. [77], we consider the Hamiltonian

$$\tilde{H} = \begin{pmatrix} 0 & \frac{b_B}{2} & 0 \\ \frac{b_B}{2} & V_+ - V_- & -\sqrt{2}t \\ 0 & -\sqrt{2}t & -\epsilon + U - V_- + \tilde{P} \end{pmatrix} + H_{ph} \quad (41)$$

in the basis $\{|(1, 1)T_0\rangle, |(1, 1)S\rangle, |(0, 2)S\rangle\}$, because the effect of $|(0, 2)S\rangle$ on the qubit lifetimes is dominating. Here $\tilde{P} = P_{SR} - P_T$, and we note that the electron-phonon interaction matrix elements P_S and P_S^\dagger have a negligible effect on T_1 and T_2 and were therefore omitted. To separate the qubit subspace from $|(0, 2)S\rangle$, we perform a fourth-order Schrieffer-Wolff transformation assuming that $|t|$ and \tilde{P} are small compared to $U - \epsilon - V_+ - |b_B|/2$. Then we apply a unitary transformation to the resulting 2×2 Hamiltonian that diagonalizes the phonon-independent part, as it was done in Sec. 3.1.4. Consequently, the $\delta B_{\tilde{x}}$ and $\delta B_{\tilde{z}}$ that we derive from the qubit Hamiltonian characterize T_1 and T_φ , respectively [see Eqs. (17)–(19)]. The parameters we use for our calculation allow us to assume $V_+ \simeq V_-$ and simplify the

expressions for $\delta B_{\tilde{x}}$ and $\delta B_{\tilde{z}}$ as follows:

$$\delta B_{\tilde{x}}(\tau) \simeq \frac{b_B t^2 [b_B^2 t^2 + 2(t^2 G_5^2 + G_5^4 - 4t^4)]}{2G_5 G_6} \tilde{P}(\tau) - \frac{b_B t^2 (G_5^2 - t^2)}{G_6} \tilde{P}^2(\tau), \quad (42)$$

$$\delta B_{\tilde{z}}(\tau) \simeq [t^2 G_5 [4t^2 (2t^2 - G_5^2) + b_B^2 (2G_5^2 - 3t^2)] \tilde{P}(\tau) + t^4 [b_B^2 + 4(G_5^2 - 2t^2)] \tilde{P}^2(\tau)] \frac{1}{2G_5 G_6}, \quad (43)$$

where we introduced

$$G_5 = U - V_+ - \epsilon, \quad (44)$$

$$G_6 = G_5^3 \sqrt{b_B^2 (t^2 - G_5^2)^2 + \frac{t^4 (b_B^2 - 8t^2 + 4G_5^2)^2}{4G_5^2}}. \quad (45)$$

Using these expressions, we will now discuss the numerical data shown in Sec. 4.1.

As a first example, we start with the remarkable decay of T_1 by two orders of magnitude seen in Fig. 11. In the dependence of T_1 on b_B the two-phonon process is dominating, especially for smaller b_B and larger temperature (for $b_B = 2 \mu\text{eV}$ and $T = 100 \text{ mK}$, $\Gamma_1^{2p}/\Gamma_1^{1p} \simeq 2.7$). To analyze this dependence we therefore consider only two-phonon process terms in $\delta B_{\tilde{x}}$, i.e., the prefactor before $\tilde{P}^2(\tau)$. From Eq. (42), we see that the numerator of the prefactor is linear in b_B . The denominator is also a function of b_B , however it is of the form $\sqrt{C_9 b_B^4 + C_{10} b_B^2 + C_{11}}$, where C_9 , C_{10} , and C_{11} are constants. Consequently, the power-law $T_1 \propto b_B^{-2}$ holds very well for $b_B < 1 \mu\text{eV}$ and slightly deviates for larger b_B .

The dependence of T_1 on the detuning ϵ plotted in Fig. 14 is more complicated. Our numerical calculations show that in this case the two-phonon process again dominates. To understand the detuning-dependence of T_1 we therefore study the prefactor before $\tilde{P}^2(\tau)$ again. For the range of ϵ presented in Fig. 14, the dependence of this prefactor on ϵ is approximately of the type $(U - V_+ - \epsilon)^{-3}$, which suggests that $T_1 \propto (U - V_+ - \epsilon)^6$. As expected from this simple estimate, the relaxation time T_1 decreases rapidly with increasing ϵ in Fig. 14. We recall that this estimate is solely based on the prefactor of $\tilde{P}^2(\tau)$ in Eq. (42). Corrections to the detuning dependence of T_1 can, e.g., be expected from the factor $\cos(\tau \Delta_{ST}/\hbar)$ in the integral of Eq. (20). As mentioned in Sec. 4.1.3, the splitting Δ_{ST} is strongly affected by ϵ for the parameters of Fig. 14.

The dependence on the tunnel coupling t is very complex. As we see from Figs. 15 and 16, both one- and two-phonon processes contribute significantly to T_1 and T_2 . However, Eqs. (42) and (43) can be greatly simplified when focusing on certain regimes. For example, we see from Fig. 16 that the two-phonon process dominates in T_1 for $T = 500 \text{ mK}$. When we analyze the prefactor before $\tilde{P}^2(\tau)$ in Eq. (42), we find that its dependence on t is relatively weak for $3 \mu\text{eV} \leq t \leq 8 \mu\text{eV}$, which is consistent with Γ_1^{2p} in Fig. 16.

4.2 Zero detuning

For the case of zero detuning, i.e., $\epsilon \simeq 0$, we have to take into account the first excited orbital states. We will therefore consider our Hamiltonian in the basis $\{|(1,1)S\rangle, |(1,1)T_0\rangle,$

$|(1,1)T_+\rangle, |(1,1)T_-\rangle, |(1^*,1)S\rangle, |(1^*,1)T_+\rangle, |(1^*,1)T_0\rangle, |(1^*,1)T_-\rangle\}$, where the asterisk indicates that the electron in the QD is in the first excited state [77],

$$\tilde{H} = \begin{pmatrix} -J_S + P_{SS} & \frac{b_B}{2} & \frac{\Omega}{\sqrt{2}} & -\frac{\Omega}{\sqrt{2}} & P_{cr}^e & \frac{\Omega_1}{\sqrt{2}} & 0 & -\frac{\Omega_1}{\sqrt{2}} \\ \frac{b_B}{2} & P_T & 0 & 0 & 0 & -\frac{\Omega_1}{\sqrt{2}} & P_{cr}^e & -\frac{\Omega_1}{\sqrt{2}} \\ \frac{\Omega}{\sqrt{2}} & 0 & E_Z + P_T & 0 & \frac{\Omega_1}{\sqrt{2}} & P_{cr}^e & -\frac{\Omega_1}{\sqrt{2}} & 0 \\ -\frac{\Omega}{\sqrt{2}} & 0 & 0 & -E_Z + P_T & -\frac{\Omega_1}{\sqrt{2}} & 0 & -\frac{\Omega_1}{\sqrt{2}} & P_{cr}^e \\ P_{cr}^{e\dagger} & 0 & \frac{\Omega_1}{\sqrt{2}} & -\frac{\Omega_1}{\sqrt{2}} & \Delta E + P^e & \frac{\Omega_2}{\sqrt{2}} & 0 & -\frac{\Omega_2}{\sqrt{2}} \\ \frac{\Omega_1}{\sqrt{2}} & -\frac{\Omega_1}{\sqrt{2}} & P_{cr}^{e\dagger} & 0 & \frac{\Omega_2}{\sqrt{2}} & \Delta E + E_Z + P^e & -\frac{\Omega_3}{\sqrt{2}} & 0 \\ 0 & P_{cr}^{e\dagger} & -\frac{\Omega_1}{\sqrt{2}} & -\frac{\Omega_1}{\sqrt{2}} & 0 & -\frac{\Omega_3}{\sqrt{2}} & \Delta E + P^e & -\frac{\Omega_3}{\sqrt{2}} \\ -\frac{\Omega_1}{\sqrt{2}} & -\frac{\Omega_1}{\sqrt{2}} & 0 & P_{cr}^{e\dagger} & -\frac{\Omega_2}{\sqrt{2}} & 0 & -\frac{\Omega_3}{\sqrt{2}} & \Delta E - E_Z + P^e \end{pmatrix} + H_{ph}. \quad (46)$$

Here, the splitting J_S takes into account the hybridization of $|(0,2)S\rangle$ and $|(2,0)S\rangle$ with $|(1,1)S\rangle$ and is defined as

$$J_S = \frac{1}{2}(\sqrt{16t^2 + (U - V_+)^2} - U - V_+ + 2V_-). \quad (47)$$

The matrix elements P^e , P_{cr}^e , $P_{cr}^{e\dagger}$ result from the electron-phonon interaction in the same way as was shown in Sec. 2.2, but for the corresponding excited states. The matrix element P_{SS} is a linear combination of electron-phonon interaction matrix elements including the effect of $|(2,0)S\rangle$ and $|(0,2)S\rangle$. The terms $\Omega_1, \Omega_2, \Omega_3$ arise from SOI. The derivation of all these matrix elements is described in detail in Ref. [77], Appendix C.

We then perform an initial unitary transformation, followed by a Schrieffer-Wolff transformation, and apply Bloch-Redfield theory as described in Sec. 2.3 and plot the temperature dependence of T_1 and T_2 , see Fig. 17. Here we take $B = 0.4$ T, $t = 24$ μ eV, $U = 1.2$ meV, $V_+ = 50$ μ eV, $V_- = 49.5$ μ eV, $\Delta E = 200$ μ eV, $L = 150$ nm, $l_R = 2$ μ m, and $b_B = -1$ μ eV. Consequently, $J_S = 1.5$ μ eV and $\Delta_{ST} = 2.5$ μ eV. Comparing Fig. 17 with Fig. 12 we see that the qubit lifetimes are several orders of magnitude longer than in the case of large detuning. This makes the zero detuning regime favorable for S - T_0 qubits, which was also shown for DQDs in GaAs/AlGaAs in our previous work [77].

The calculations for Fig. 17 were done with the orbital excitation along the axis that connects the QDs. The decay rates resulting from excitation along the orthogonal direction do not change the qualitative picture, which is sufficient for our consideration. For Fig. 17 we chose $\eta = 0$. If we take $\eta = \pi/2$, the rates are either smaller or of the same order as for $\eta = 0$. States of type $(1, 1^*)$ with the excited electron in the right QD will change the results only by factors around 2, and therefore were not included for simplicity.

The valley degrees of freedom were neglected in our

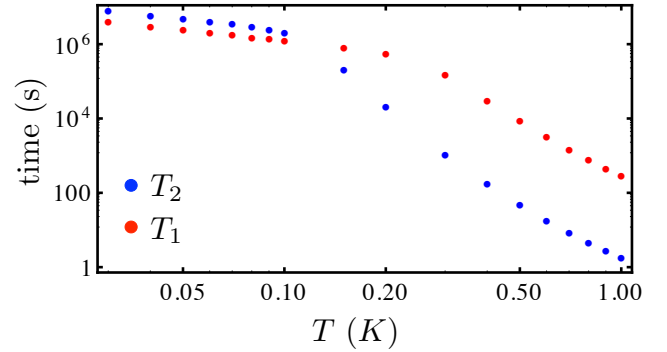


Figure 17: The dependence of T_2 and T_1 of a S - T_0 qubit on temperature for the unbiased case $\epsilon \simeq 0$. The parameters are provided in Sec. 4.2.

model because valley splittings around 1 meV were already realized experimentally [57–59], which is a large gap compared to the orbital level spacing $\Delta E = 200$ μ eV. While valley-related effects are strongly suppressed when the valley splitting is large, we note that they can be a significant source of decoherence when the splitting is small [52, 53, 70, 93, 110]. Therefore, setups with a large valley splitting are usually favorable when implementing spin qubits in Si/SiGe heterostructures, which is the case that we focus on in this work.

5 Comparison with other decay mechanisms

In our previous calculations for S - T_0 qubits in GaAs DQDs [77], we found that the considered one- and two-phonon processes may very well correspond to the dominant decay

channels in an experiment. In contrast, for the Si DQDs studied here, the obtained decay times for singlet-triplet qubits are relatively long, at least for many parameter regimes. We note that this finding is consistent with a recent analysis of resonant exchange qubits in three-electron triple quantum dots [92], where the relaxation times due to phonons were predicted to be orders of magnitude longer in Si than in GaAs. Consequently, it is well possible that the experimentally feasible qubit lifetimes will be limited by other mechanisms, some of which we briefly discuss below. Nevertheless, even if other mechanisms turn out to dominate in standard regimes for qubit operation, we identified and proposed ways how our theory can be confirmed experimentally, which would be a desirable contribution to understanding and assessing the role of the discussed one- and two-phonon processes in Si-based systems.

Among the most relevant noise sources for electrically controllable qubits is charge noise [111–113], which may be due to charge traps within the heterostructure or noise from the gates. For instance, electrical noise was considered as a major obstacle for the implementation of high-quality two-qubit gates between S - T_0 qubits in GaAs [14]. Theoretical studies suggest that the effects of charge noise in GaAs and Si are similar to a great extent [114, 115]. As evident from, e.g., the pure-dephasing model discussed in Ref. [116], the resulting decay will depend both on the spectral density of the noisy fluctuations in the level splitting of the qubit and on the details of the operation scheme, as suitable pulse sequences for dynamical decoupling may strongly prolong the dephasing time [11, 13, 14, 117–119]. Furthermore, decoherence due to charge noise can be much suppressed by operating the qubit at a sweet spot, where the level splitting of the qubit is insensitive to electric field fluctuations. This is a particularly advantageous feature of S - T_0 qubits in unbiased DQDs [1, 4, 22, 120] and S - T_- qubits (especially those based on $|(1, 1)T'_- \rangle$ - $|(1, 1)S' \rangle$, see Sec. 3.2) operated at the anticrossing [18, 74].

While we considered here the Bloch-Redfield theory and studied the phonon-assisted relaxation and decoherence that results from one- and two-phonon processes, such as the two-phonon Raman process [102–107], a spin-boson model was adopted in Ref. [91] in order to describe pure dephasing of S - T_0 qubits in the absence of any real or virtual phonon absorption or emission. In the calculations of Ref. [91], interactions between the electrons and a dissipative phonon reservoir lead to an exponential decay of the qubit coherence, and the associated dephasing time depends strongly on the overlap of the electron wave functions and the decay properties of the phonon bath. In contrast to our model, where the qubit lifetimes in GaAs turned out to be limited by the piezoelectric electron-phonon coupling [77], the lifetimes calculated in Ref. [91] for both Si and GaAs are limited by the deformation potential coupling. Depending on the experimental setup this additional decay channel might domi-

nate, particularly for strongly overlapping quantum dots in Si, and it can be suppressed by moving the two dots farther apart [91].

As mentioned before in Sec. 4.2, valley-related effects can become an important source of decoherence if the energy splitting between valleys is not sufficiently large [53, 70, 110]. Among other things, disorder or interface effects for Si/SiGe and Si/SiO₂ can play a significant role here [53, 110, 121–124]. When the valley splitting is large, however, qubit decoherence due to the valley degrees of freedom is suppressed, and splittings of the order of 1 meV or even more are experimentally feasible [56–59, 125].

Finally, the coherence of qubits in Si/SiGe heterostructures can be lost due to interaction with the nuclear spins, although the hyperfine-induced dephasing time of 360 ns (no echo pulses) reported for a Si DQD [62] is already one to two orders of magnitude longer than the typical values for GaAs [6–8, 11]. Ultimately, however, the hyperfine coupling will not present a limiting factor for the qubit lifetimes, since Si and Ge can be grown nuclear-spin-free.

6 Conclusions

We considered S - T_- qubits in the anticrossing region for the two cases where the singlet is mainly $|(0, 2)S \rangle$ and where it is mainly $|(1, 1)S \rangle$. In the latter case, T_1 and T_2 turned out to be much longer than in the former one. We showed that the magnetic field gradient reduces T_1 and T_2 substantially, when it is above a certain value at which the one-phonon process starts to dominate over the two-phonon process. This follows from the fact that the magnetic field gradient provides the splitting in the anticrossing, and therefore the one-phonon process is very sensitive to its change. In contrast, two-phonon-based relaxation does not change noticeably in the range of parameters we use, and two-phonon-based dephasing is very weak even though it does depend on the magnetic field gradient. We proposed regimes where our theory of one- and two-phonon processes may be experimentally tested. Remarkably, T_2 (T_1) has a peak (dip) at the center of the S - T_- anticrossing in the dependence on the applied magnetic field (Fig. 8). As the external magnetic field can easily be changed in an experiment, this peak (dip) might be an experimental indication of the center of the anticrossing, which is a regime of interest e.g. for Refs. [18, 74].

We also studied S - T_0 qubits in the regimes which were presented in our previous work on DQDs in GaAs/AlGaAs [77], i.e., at large detuning in the anticrossing region of the singlets and at zero detuning. The key result that small detuning is much more favorable regarding the qubit lifetimes than large detuning is valid here too. We showed that in the anticrossing region even small changes in ϵ may shorten T_1 and T_2 by two orders of magnitude. We note that the relation $T_\varphi \ll T_1$, shown in our previous work for the regime

of large detuning, does not hold for the usual parameters of experiments with SiGe/Si/SiGe DQDs because of a rather large applied magnetic field gradient. We showed that the magnetic field gradient can reduce T_1 by orders of magnitude. We demonstrated that the dependence of T_1 on tunnel coupling is qualitatively different for different temperatures, which is explained by the behavior of one- and two-phonon processes. Our study of the effect of various system parameters on T_1 and T_2 shows ways how to prolong the phonon-based decoherence and relaxation times by orders of magnitude.

Acknowledgments

We thank S. Chesi, S. N. Coppersmith, M. Friesen, T. Otsuka, K. Takeda, and J. R. Wootton for helpful discussions and acknowledge support from the Swiss National Science Foundation, NCCR QSIT, SiSPIN, the ITNs S³NANO and Spin-NANO, and IARPA.

References

- [1] D. Loss and D. P. DiVincenzo, *Phys. Rev. A* **57**, 120 (1998).
- [2] R. Hanson, L. P. Kouwenhoven, J. R. Petta, S. Tarucha, and L. M. K. Vandersypen, *Rev. Mod. Phys.* **79**, 1217 (2007).
- [3] C. Kloeffer and D. Loss, *Annu. Rev. Condens. Matter Phys.* **4**, 51 (2013).
- [4] G. Burkard, D. Loss, and D. P. DiVincenzo, *Phys. Rev. B* **59**, 2070 (1999).
- [5] J. Levy, *Phys. Rev. Lett.* **89**, 147902 (2002).
- [6] A. V. Khaetskii, D. Loss, and L. Glazman, *Phys. Rev. Lett.* **88**, 186802 (2002).
- [7] I. A. Merkulov, A. L. Efros, and M. Rosen, *Phys. Rev. B* **65**, 205309 (2002).
- [8] W. A. Coish and D. Loss, *Phys. Rev. B* **70**, 195340 (2004).
- [9] A. C. Johnson, J. R. Petta, J. M. Taylor, A. Yacoby, M. D. Lukin, C. M. Marcus, M. P. Hanson, and A. C. Gossard, *Nature (London)* **435**, 925 (2005).
- [10] J. M. Taylor, H.-A. Engel, W. Dür, A. Yacoby, C. M. Marcus, P. Zoller, and M. D. Lukin, *Nat. Phys.* **1**, 177 (2005).
- [11] J. R. Petta, A. C. Johnson, J. M. Taylor, E. A. Laird, A. Yacoby, M. D. Lukin, C. M. Marcus, M. P. Hanson, and A. C. Gossard, *Science* **309**, 2180 (2005).
- [12] S. Foletti, H. Bluhm, D. Mahalu, V. Umansky, and A. Yacoby, *Nat. Phys.* **5**, 903 (2009).
- [13] H. Bluhm, S. Foletti, I. Neder, M. Rudner, D. Mahalu, V. Umansky, and A. Yacoby, *Nat. Phys.* **7**, 109 (2011).
- [14] M. D. Shulman, O. E. Dial, S. P. Harvey, H. Bluhm, V. Umansky, and A. Yacoby, *Science* **336**, 202 (2012).
- [15] J. Klinovaja, D. Stepanenko, B. I. Halperin, and D. Loss, *Phys. Rev. B* **86**, 085423 (2012).
- [16] J. Yoneda, T. Otsuka, T. Nakajima, T. Takakura, T. Obata, M. Pioro-Ladrière, H. Lu, C. J. Palmstrøm, A. C. Gossard, and S. Tarucha, *Phys. Rev. Lett.* **113**, 267601 (2014).
- [17] P. Scarlino, E. Kawakami, P. Stano, M. Shafiei, C. Reichl, W. Wegscheider, and L. M. K. Vandersypen, *Phys. Rev. Lett.* **113**, 256802 (2014).
- [18] S. Chesi, Y.-D. Wang, J. Yoneda, T. Otsuka, S. Tarucha, and D. Loss, *Phys. Rev. B* **90**, 235311 (2014).
- [19] P. Cerfontaine, T. Botzem, D. P. DiVincenzo, and H. Bluhm, *Phys. Rev. Lett.* **113**, 150501 (2014).
- [20] D. E. F. Biesinger, C. P. Scheller, B. Braunecker, J. Zimmerman, A. C. Gossard, and D. M. Zumbühl, *Phys. Rev. Lett.* **115**, 106804 (2015).
- [21] M. P. Wardrop and A. C. Doherty, *Phys. Rev. B* **93**, 075436 (2016).
- [22] F. Martins, F. K. Malinowski, P. D. Nissen, E. Barnes, S. Fallahi, G. C. Gardner, M. J. Manfra, C. M. Marcus, and F. Kuemmeth, *Phys. Rev. Lett.* **116**, 116801 (2016).
- [23] R. Maurand, X. Jehl, D. Kotekar-Patil, A. Corna, H. Bohuslavskiy, R. Laviéville, L. Hutin, S. Barraud, M. Vinet, M. Sanquer, and S. De Franceschi, *Nat. Commun.* **7**, 13575 (2016).
- [24] H. Watzinger, C. Kloeffer, L. Vukusic, M. D. Rossell, V. Sessi, J. Kukucka, R. Kirchschrager, E. Lausecker, A. Truhlar, M. Glaser, A. Rastelli, A. Fuhrer, D. Loss, and G. Katsaros, *Nano Lett.* **16**, 6879 (2016).
- [25] C. Kloeffer, M. Trif, and D. Loss, *Phys. Rev. B* **84**, 195314 (2011).
- [26] Y. Hu, F. Kuemmeth, C. M. Lieber, and C. M. Marcus, *Nat. Nanotechnol.* **7**, 47 (2012).
- [27] F. Maier, C. Kloeffer, and D. Loss, *Phys. Rev. B* **87**, 161305(R) (2013).
- [28] C. Kloeffer, M. Trif, P. Stano, and D. Loss, *Phys. Rev. B* **88**, 241405(R) (2013).
- [29] M. Brauns, J. Ridderbos, A. Li, E. P. A. M. Bakkers, and F. A. Zwanenburg, *Phys. Rev. B* **93**, 121408(R) (2016).
- [30] A. Laucht, R. Kalra, J. T. Muhonen, J. P. Dehollain, F. A. Mohiyaddin, F. Hudson, J. C. McCallum, D. N. Jamieson, A. S. Dzurak, and A. Morello, *Appl. Phys. Lett.* **104**, 092115 (2014).
- [31] A. M. Tyryshkin, S. Tojo, J. J. L. Morton, H. Riemann, N. V. Abrosimov, P. Becker, H.-J. Pohl, T. Schenkel, M. L. W. Thewalt, K. M. Itoh, and S. A. Lyon, *Nat. Mater.* **11**, 143 (2012).
- [32] S. J. Hile, M. G. House, E. Peretz, J. Verduijn, D. Widmann, T. Kobayashi, S. Rogge, and M. Y. Simmons, *Appl. Phys. Lett.* **107**, 93504 (2015).

- [33] T. F. Watson, B. Weber, M. G. House, H. Büch, and M. Y. Simmons, *Phys. Rev. Lett.* **115**, 166806 (2015).
- [34] Y. Wang, C.-Y. Chen, G. Klimeck, M. Y. Simmons, and R. Rahman, arXiv:1703.05370.
- [35] J. J. Pla, F. A. Mohiyaddin, K. Y. Tan, J. P. Dehollain, R. Rahman, G. Klimeck, D. N. Jamieson, A. S. Dzurak, and A. Morello, *Phys. Rev. Lett.* **113**, 246801 (2014).
- [36] B. E. Kane, *Nature* **393**, 133 (1998).
- [37] M. Steger, K. Saeedi, M. L. W. Thewalt, J. J. L. Morton, H. Riemann, N. V. Abrosimov, P. Becker, and H.-J. Pohl, *Science* **336**, 1280 (2012).
- [38] K. Saeedi, S. Simmons, J. Z. Salvail, P. Dluhy, H. Riemann, N. V. Abrosimov, P. Becker, H.-J. Pohl, J. J. Morton, and M. L. Thewalt, *Science* **342**, 830 (2013).
- [39] M. Usman, C. D. Hill, R. Rahman, G. Klimeck, M. Y. Simmons, S. Rogge, and L. C. L. Hollenberg, *Phys. Rev. B* **91**, 245209 (2015).
- [40] C. D. Hill, E. Peretz, S. J. Hile, M. G. House, M. Fuechsle, S. Rogge, M. Y. Simmons, and L. C. L. Hollenberg, *Science Advances* **1**, e1500707 (2015).
- [41] J. T. Muhonen, J. P. Dehollain, A. Laucht, S. Simmons, R. Kalra, F. E. Hudson, D. N. Jamieson, J. C. McCallum, K. M. Itoh, A. S. Dzurak, and A. Morello, arXiv:1702.07991.
- [42] G. W. Morley, P. Lueders, M. H. Mohammady, S. J. Balian, G. Aeppli, C. W. M. Kay, W. M. Witzel, G. Jeschke, and T. S. Monteiro, *Nat. Mater.* **12**, 103 (2013).
- [43] J. T. Muhonen, A. Laucht, S. Simmons, J. P. Dehollain, R. Kalra, F. E. Hudson, S. Freer, K. M. Itoh, D. N. Jamieson, J. C. McCallum, A. S. Dzurak, and A. Morello, *J. Phys. Condens. Matter* **27**, 154205 (2015).
- [44] M. Veldhorst, C. H. Yang, J. C. C. Hwang, W. Huang, J. P. Dehollain, J. T. Muhonen, S. Simmons, A. Laucht, F. E. Hudson, K. M. Itoh, A. Morello, and A. S. Dzurak, *Nature* **526**, 410 (2015).
- [45] M. J. Calderón, B. Koiller, X. Hu, and S. Das Sarma, *Phys. Rev. Lett.* **96**, 096802 (2006).
- [46] K. Takeda, T. Obata, Y. Fukuoka, W. M. Akhtar, J. Kamioka, T. Kadera, S. Oda, and S. Tarucha, *Appl. Phys. Lett.* **102**, 123113 (2013).
- [47] E. Kawakami, P. Scarlino, D. R. Ward, F. R. Braakman, D. E. Savage, M. G. Lagally, M. Friesen, S. N. Coppersmith, M. A. Eriksson, and L. M. K. Vandersypen, *Nat. Nanotechnol.* **9**, 666 (2014).
- [48] D. M. Zajac, T. M. Hazard, X. Mi, K. Wang, and J. R. Petta, *Appl. Phys. Lett.* **106**, 223507 (2015).
- [49] K. Takeda, J. Kamioka, T. Otsuka, J. Yoneda, T. Nakajima, M. R. Delbecq, S. Amaha, G. Allison, T. Kadera, S. Oda, and S. Tarucha, *Sci. Adv.* **2**, e1600694 (2016).
- [50] D. M. Zajac, A. J. Sigillito, M. Russ, F. Borjans, J. M. Taylor, G. Burkard, and J. R. Petta, *Science* **359**, 439 (2018).
- [51] T. F. Watson, S. G. J. Philips, E. Kawakami, D. R. Ward, P. Scarlino, M. Veldhorst, D. E. Savage, M. G. Lagally, M. Friesen, S. N. Coppersmith, M. A. Eriksson, and L. M. K. Vandersypen, *Nature* **555**, 633 (2018).
- [52] J. K. Gamble, M. Friesen, S. N. Coppersmith, and X. Hu, *Phys. Rev. B* **86**, 035302 (2012).
- [53] C. Tahan and R. Joynt, *Phys. Rev. B* **89**, 075302 (2014).
- [54] F. Schäffler, *Semicond. Sci. Technol.* **12**, 1515 (1997).
- [55] M. Friesen, S. Chutia, C. Tahan, and S. N. Coppersmith, *Phys. Rev. B* **75**, 115318 (2007).
- [56] F. A. Zwanenburg, A. S. Dzurak, A. Morello, M. Y. Simmons, L. C. L. Hollenberg, G. Klimeck, S. Rogge, S. N. Coppersmith, and M. A. Eriksson, *Rev. Mod. Phys.* **85**, 961 (2013).
- [57] S. Goswami, K. A. Slinker, M. Friesen, L. M. McGuire, J. L. Truitt, C. Tahan, L. J. Klein, J. O. Chu, P. M. Mooney, D. W. van der Weide, R. Joynt, S. N. Coppersmith, and M. A. Eriksson, *Nat. Phys.* **3**, 41 (2007).
- [58] M. Xiao, M. G. House, and H. W. Jiang, *Appl. Phys. Lett.* **97**, 032103 (2010).
- [59] C. H. Yang, A. Rossi, R. Ruskov, N. S. Lai, F. A. Mohiyaddin, S. Lee, C. Tahan, G. Klimeck, A. Morello, and A. S. Dzurak, *Nat. Commun.* **4**, 2069 (2013).
- [60] M. Prada, R. H. Blick, and R. Joynt, *Phys. Rev. B* **77**, 115438 (2008).
- [61] M. Raith, P. Stano, and J. Fabian, *Phys. Rev. B* **86**, 205321 (2012).
- [62] B. M. Maune, M. G. Borselli, B. Huang, T. D. Ladd, P. W. Deelman, K. S. Holabird, A. A. Kiselev, I. Alvarado-Rodriguez, R. S. Ross, A. E. Schmitz, M. Sokolich, C. A. Watson, M. F. Gyure, and A. T. Hunter, *Nature (London)* **481**, 344 (2012).
- [63] J. R. Prance, Z. Shi, C. B. Simmons, D. E. Savage, M. G. Lagally, L. R. Schreiber, L. M. K. Vandersypen, M. Friesen, R. Joynt, S. N. Coppersmith, and M. A. Eriksson, *Phys. Rev. Lett.* **108**, 046808 (2012).
- [64] D. Culcer, L. Cywiński, Q. Li, X. Hu, and S. Das Sarma, *Phys. Rev. B* **80**, 205302 (2009).
- [65] J.-T. Hung, L. Cywiński, X. Hu, and S. Das Sarma, *Phys. Rev. B* **88**, 085314 (2013).
- [66] L. V. C. Assali, H. M. Petrilli, R. B. Capaz, B. Koiller, X. Hu, and S. Das Sarma, *Phys. Rev. B* **83**, 165301 (2011).
- [67] D. Culcer, A. L. Saraiva, B. Koiller, X. Hu, and S. Das Sarma, *Phys. Rev. Lett.* **108**, 126804 (2012).
- [68] C. B. Simmons, J. R. Prance, B. J. Van Bael, T. S. Koh, Z. Shi, D. E. Savage, M. G. Lagally, R. Joynt,

- M. Friesen, S. N. Coppersmith, and M. A. Eriksson, *Phys. Rev. Lett.* **106**, 156804 (2011).
- [69] A. M. Tyryshkin, S. A. Lyon, T. Schenkel, J. Bokor, J. Chu, W. Jantsch, F. Schäffler, J. L. Truitt, S. N. Coppersmith, and M. A. Eriksson, *Physica E* **35**, 257 (2006).
- [70] C. Tahan, M. Friesen, and R. Joynt, *Phys. Rev. B* **66**, 035314 (2002).
- [71] B. A. Glavin and K. W. Kim, *Phys. Rev. B* **68**, 045308 (2003).
- [72] L. Wang and M. W. Wu, *J. Appl. Phys.* **110**, 043716 (2011).
- [73] L. Wang, K. Shen, B. Y. Sun, and M. W. Wu, *Phys. Rev. B* **81**, 235326 (2010).
- [74] C. H. Wong, M. A. Eriksson, S. N. Coppersmith, and M. Friesen, *Phys. Rev. B* **92**, 045403 (2015).
- [75] X. Wu, D. R. Ward, J. R. Prance, D. Kim, J. K. Gamble, R. T. Mohr, Z. Shi, D. E. Savage, M. G. Lagally, M. Friesen, S. N. Coppersmith, and M. A. Eriksson, *Proc. Natl. Acad. Sci. USA* **111**, 11938 (2014).
- [76] Y.-S. Shin, T. Obata, Y. Tokura, M. Pioro-Ladrière, R. Brunner, T. Kubo, K. Yoshida, and S. Tarucha, *Phys. Rev. Lett.* **104**, 046802 (2010).
- [77] V. Kornich, C. Kloeffer, and D. Loss, *Phys. Rev. B* **89**, 085410 (2014).
- [78] A. V. Khaetskii and Y. V. Nazarov, *Phys. Rev. B* **61**, 12639 (2000).
- [79] I. L. Aleiner and V. I. Fal'ko, *Phys. Rev. Lett.* **87**, 256801 (2001).
- [80] V. N. Golovach, A. V. Khaetskii, and D. Loss, *Phys. Rev. Lett.* **93**, 016601 (2004).
- [81] P. Stano and J. Fabian, *Phys. Rev. B* **72**, 155410 (2005).
- [82] P. Stano and J. Fabian, *Phys. Rev. Lett.* **96**, 186602 (2006).
- [83] C. Herring and E. Vogt, *Phys. Rev.* **101**, 944 (1956).
- [84] P. Y. Yu and M. Cardona, *Fundamentals of Semiconductors: Physics and Material Properties*, 4th ed. (Springer, Berlin, 2010).
- [85] A. N. Cleland, *Foundations of Nanomechanics: From Solid-State Theory to Device Applications* (Springer, Berlin, 2003).
- [86] S. Adachi, *Properties of Group-IV, III-V and II-VI Semiconductors* (John Wiley & Sons, Chichester, 2005).
- [87] D. Stepanenko, M. Rudner, B. I. Halperin, and D. Loss, *Phys. Rev. B* **85**, 075416 (2012).
- [88] C. P. Slichter, *Principles of Magnetic Resonance* (Springer, Berlin, 1980).
- [89] M. Borhani, V. N. Golovach, and D. Loss, *Phys. Rev. B* **73**, 155311 (2006).
- [90] R. Winkler, *Spin-Orbit Coupling Effects in Two-Dimensional Electron and Hole Systems* (Springer, Berlin, 2003).
- [91] X. Hu, *Phys. Rev. B* **83**, 165322 (2011).
- [92] V. Srinivasa, J. M. Taylor, and C. Tahan, *Phys. Rev. B* **94**, 205421 (2016).
- [93] N. Rohling and G. Burkard, *New J. Phys.* **14**, 083008 (2012).
- [94] H. Ribeiro, J. R. Petta, and G. Burkard, *Phys. Rev. B* **82**, 115445 (2010).
- [95] J. R. Petta, H. Lu, and A. C. Gossard, *Science* **327**, 669 (2010).
- [96] H. Ribeiro, G. Burkard, J. R. Petta, H. Lu, and A. C. Gossard, *Phys. Rev. Lett.* **110**, 086804 (2013).
- [97] H. Ribeiro, J. R. Petta, and G. Burkard, *Phys. Rev. B* **87**, 235318 (2013).
- [98] Z. Wilamowski, W. Jantsch, H. Malissa, and U. Rössler, *Phys. Rev. B* **66**, 195315 (2002).
- [99] L. Vervoort, R. Ferreira, and P. Voisin, *Phys. Rev. B* **56**, R12744 (1997).
- [100] L. Vervoort, R. Ferreira, and P. Voisin, *Semicond. Sci. Technol.* **14**, 227 (1999).
- [101] M. O. Nestoklon, E. L. Ivchenko, J.-M. Jancu, and P. Voisin, *Phys. Rev. B* **77**, 155328 (2008).
- [102] D. E. McCumber and M. D. Sturge, *J. Appl. Phys.* **34**, 1682 (1963).
- [103] W. M. Yen, W. C. Scott, and A. L. Schawlow, *Phys. Rev.* **136**, A271 (1964).
- [104] S. B. Altner, G. Zumofen, U. P. Wild, and M. Mit-sunaga, *Phys. Rev. B* **54**, 17493 (1996).
- [105] R. S. Meltzer, in *Spectroscopic Properties of Rare Earths in Optical Materials*, edited by G. Liu and B. Jacquier (Springer, Berlin, 2005), Chap. 4, pp. 191–265.
- [106] K. Roszak and P. Machnikowski, *Phys. Rev. B* **80**, 195315 (2009).
- [107] V. Kornich, C. Kloeffer, and D. Loss, *Phys. Rev. B* **90**, 079901(E) (2014).
- [108] T. Meunier, I. T. Vink, L. H. Willems van Beveren, K.-J. Tielrooij, R. Hanson, F. H. L. Koppens, H. P. Tranitz, W. Wegscheider, L. P. Kouwenhoven, and L. M. K. Vandersypen, *Phys. Rev. Lett.* **98**, 126601 (2007).
- [109] V. N. Golovach, A. V. Khaetskii, and D. Loss, *Phys. Rev. B* **77**, 045328 (2008).
- [110] D. Culcer, L. Cywiński, Q. Li, X. Hu, and S. Das Sarma, *Phys. Rev. B* **82**, 155312 (2010).
- [111] A. V. Kuhlmann, J. Houel, A. Ludwig, L. Greuter, D. Reuter, A. D. Wieck, M. Poggio, and R. J. Warburton, *Nat. Phys.* **9**, 570 (2013).
- [112] O. E. Dial, M. D. Shulman, S. P. Harvey, H. Bluhm, V. Umansky, and A. Yacoby, *Phys. Rev. Lett.* **110**, 146804 (2013).
- [113] D. Kim, D. R. Ward, C. B. Simmons, J. K. Gamble, R. Blume-Kohout, E. Nielsen, D. E. Savage, M. G. Lagally, M. Friesen, S. N. Coppersmith, and M. A. Eriksson, *Nat. Nanotechnol.* **10**, 243 (2015).

- [114] X. Hu and S. Das Sarma, [Phys. Rev. Lett. **96**, 100501 \(2006\)](#).
- [115] D. Culcer, X. Hu, and S. Das Sarma, [Appl. Phys. Lett. **95**, 073102 \(2009\)](#).
- [116] L. Cywiński, R. M. Lutchyn, C. P. Nave, and S. Das Sarma, [Phys. Rev. B **77**, 174509 \(2008\)](#).
- [117] L. Viola, S. Lloyd, and E. Knill, [Phys. Rev. Lett. **83**, 4888 \(1999\)](#).
- [118] C. Barthel, J. Medford, C. M. Marcus, M. P. Hanson, and A. C. Gossard, [Phys. Rev. Lett. **105**, 266808 \(2010\)](#).
- [119] D. Kim, D. R. Ward, C. B. Simmons, D. E. Savage, M. G. Lagally, M. Friesen, S. N. Coppersmith, and M. A. Eriksson, [npj Quantum Inf. **1**, 15004 \(2015\)](#).
- [120] M. D. Reed, B. M. Maune, R. W. Andrews, M. G. Borselli, K. Eng, M. P. Jura, A. A. Kiselev, T. D. Ladd, S. T. Merkel, I. Milosavljevic, E. J. Pritchett, M. T. Rakher, R. S. Ross, A. E. Schmitz, A. Smith, J. A. Wright, M. F. Gyure, and A. T. Hunter, [Phys. Rev. Lett. **116**, 110402 \(2016\)](#).
- [121] A. L. Saraiva, M. J. Calderón, R. B. Capaz, X. Hu, S. Das Sarma, and B. Koiller, [Phys. Rev. B **84**, 155320 \(2011\)](#).
- [122] M. O. Nestoklon, L. E. Golub, and E. L. Ivchenko, [Phys. Rev. B **73**, 235334 \(2006\)](#).
- [123] S. Chutia, S. N. Coppersmith, and M. Friesen, [Phys. Rev. B **77**, 193311 \(2008\)](#).
- [124] J. K. Gamble, M. A. Eriksson, S. N. Coppersmith, and M. Friesen, [Phys. Rev. B **88**, 035310 \(2013\)](#).
- [125] T. B. Boykin, G. Klimeck, M. A. Eriksson, M. Friesen, S. N. Coppersmith, P. von Allmen, F. Oya-fuso, and S. Lee, [Appl. Phys. Lett. **84**, 115 \(2004\)](#).